Scilight

Sustainable Engineering Novit

https://www.sciltp.com/journals/sen

Review

Check for updates

Metal Halide Perovskites: From Nanocrystals to Superlattices

Rujiao Dong [1,2], Jin-Wook Lee [3] and Rui Wang [1,*]

[1] Department of Materials Science and Engineering, School of Engineering, Westlake University, Hangzhou 310030, China
[2] State Key Laboratory of Silicon and Advanced Semiconductor Materials and School of Materials Science and Engineering, Zhejiang University, Hangzhou 310027, China
[3] School of Transdisciplinary Innovations, Seoul National University, Seoul 08826, Republic of Korea
* Correspondence: wangrui@westlake.edu.cn

How To Cite: Dong, R.; Lee, J.-W.; Wang, R. Metal Halide Perovskites: From Nanocrystals to Superlattices. *Sustainable Engineering Novit* **2026**, *2*(2), 2. https://doi.org/10.53941/sen.2026.100007

Received: 22 January 2026
Revised: 9 March 2026
Accepted: 19 March 2026
Published: 14 May 2026

Abstract: Metal halide perovskites (MHPs), in the form of nanocrystals (NCs) and their superlattices (SLs), have attracted substantial attention owing to their outstanding optoelectronic properties, solution processability, and emergent collective phenomena. In particular, MHP NCs, characterized by bright triplet excitons, slow exciton dephasing, and minimal spectral inhomogeneity, constitute an ideal platform for investigating collective coupling. This review provides a concise overview of MHP NCs and SLs, ranging from assembly-unit design to functional supermaterials. Starting from individual MHP NCs, this review summarizes recent advances in SL formation and structural diversity, highlights key collective optoelectronic phenomena, and discusses representative device applications.

Keywords: perovskite nanocrystals; self-assembly; superlattices; superfluorescence

1. Introduction

Metal halide perovskites (MHPs) constitute a versatile class of optoelectronic materials whose exceptional properties, including high absorption coefficients, long carrier diffusion lengths, and defect-tolerant electronic structures [1,2], have driven rapid advances in photovoltaics [3–14], light-emitting diodes (LEDs) [15–31], photodetectors [32,33], and related technologies [32,34–38]. At the nanoscale, perovskites exhibit characteristics distinct from both their bulk counterparts and conventional semiconductor quantum dots (QDs) [39–41]. The reduction in dimensionality imposes quantum confinement [42–44], discretizing electronic states and enabling size-dependent bandgap modulation that affords broad spectral tunability [45–48]. Beyond these quantum size effects, their most distinctive attribute lies in their intrinsic defect tolerance [49,50]. Unlike conventional CdSe or InP QDs, which require sophisticated core-shell architectures to suppress deep trap states arising from surface defects [40], perovskite nanocrystals (PNCs) inherently suppress deep-level defect formation and preserve near-unity photoluminescence quantum yields (PLQYs) even without post-synthetic passivation [49,51–53], rendering them highly attractive for LED applications.

Beyond these intrinsic features, PNCs exhibit controllable aggregation and self-organization, making them ideal "artificial atoms" with multidimensional adjustability. As building blocks for self-assembled structures, NCs introduce design principles distinct from conventional atomic crystals: they come in varied sizes and morphologies and assemble through weak interactions instead of strong chemical bonds, facilitating the creation of novel architectures like moiré [54–56] and kagome [57] superlattices (SLs). Furthermore, owing to their intrinsically tunable characteristics, NCs can give rise to assemblies that display emergent properties unattainable in isolated NCs. For instance, PNCs support bright triplet excitons characterized by high oscillator strength [58], long coherence times, and minimal inhomogeneous broadening [2,59], rendering their ordered SLs a promising platform for exploring collective optical effects, such as superfluorescence (SF). These phenomena hold great promise for advanced optoelectronic devices, potentially enabling higher-efficiency light emission, ultrafast energy transport, and novel quantum light sources [60].

Despite the rapid growth of the field, a disconnect persists in the literature. Existing reviews on PNCs largely focus on structure-property-application relationships at the single-particle level, with limited consideration of ordered collective states [20,40,49,61–67]. Conversely, studies on SLs often emphasize assembly behavior and resulting optical fingerprints, centering on structure-coupling-collective responses while downplaying the materials-specific origins of the building blocks [68–72]. This fragmented perspective hinders the rational design of functional SL materials from the bottom up, creating a knowledge gap between NC engineering and supermaterials.

To bridge this gap, this review aims to establish a unified framework. We systematically discuss: (i) the design principles of PNC building blocks, (ii) the formation mechanisms and structural diversity of MHP SLs, (iii) their collective optoelectronic properties and underlying physics, and (iv) emerging applications. Finally, we conclude with an outlook on key challenges and future opportunities.

2. MHP NCs

PNCs can be regarded as "artificial atoms" for constructing supermaterials, as their intrinsic single-particle properties dictate the emergent macroscopic behaviors and functionalities of the assembled structures. A rigorous understanding of these fundamental characteristics is therefore indispensable for interpreting and engineering collective phenomena in PNC SLs. In this chapter, we provide an overview of the essential properties of PNCs, laying the foundation for subsequent discussions on their self-assembly and collective optoelectronic behavior.

2.1. Crystal Structure and Intrinsic Lattice Properties

MHPs typically adopt the ABX_3 stoichiometry (where A = Cs^+, $CH_3NH_3^+$ (MA^+), $HC(NH_2)_2^+$ (FA^+); B = Pb^{2+}; X = Cl^-, Br^-, I^-, or their mixtures). Their three-dimensional (3D) crystal framework is constructed from corner-sharing $[PbX_6]^{4-}$ octahedra, with A-site cations occupying the twelve-coordinated cavities between adjacent octahedra. At the nanoscale, these structures commonly exhibit cubic or orthorhombic symmetry (Figure 1a). A representative high-angle annular dark-field scanning transmission electron microscopy (HAADF-STEM) image of a single cube-shaped $CsPbBr_3$ NC further illustrates the well-defined crystalline lattice at the single-particle level (Figure 1c) [40]. Owing to their large, polarizable A- and B-site cations and relatively low-charged X-site anions, the internal Coulomb interactions are weak, giving rise to a pronounced soft lattice characteristic [39]. This structural softness enables low-temperature, solution-phase synthesis, which is difficult to achieve in conventional covalent semiconductor NCs. At the same time, the flexible lattice facilitates dynamic surface reconstruction, which plays a crucial role in surface functionalization, ligand binding, and post-synthetic treatments of PNCs [40,63,73,74]. Another defining feature of MHPs is their remarkable defect tolerance: although numerous defects are present, they rarely form deep-level trap states within the bandgap (Figure 1b) [63,67]. As a result, nonradiative recombination is effectively suppressed even in the presence of a relatively high defect density. Such tolerance allows the fabrication of PNCs under mild conditions compared with other semiconductor NCs and accounts for their highly efficient photoluminescence (Figure 1d) [46,51,52].

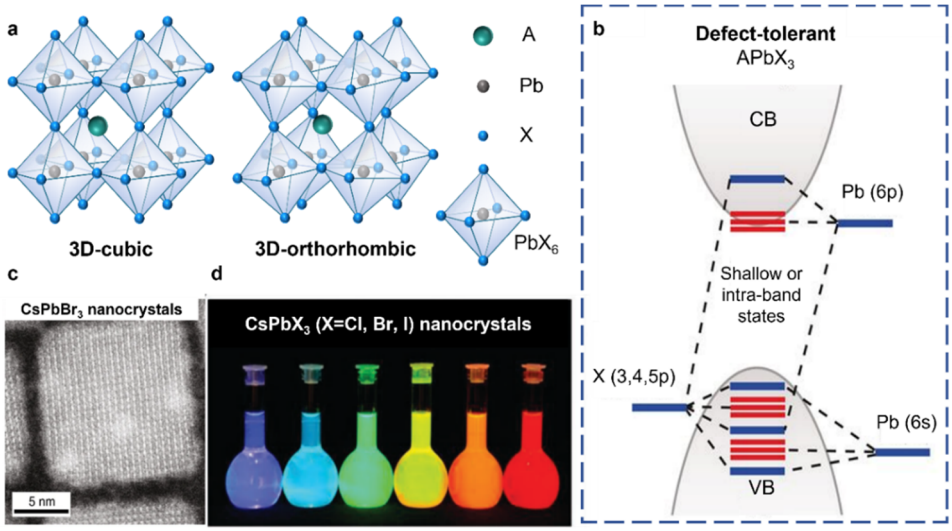

Figure 1. Basic Properties of MHP NCs. (**a**) 3D cubic and orthorhombic perovskite lattices. (**b**) Defect tolerance in lead halide PNCs. Reprinted with permission from Ref. [67]. Copyright 2017, American Association for the Advancement of Science. (**c**) HAADF-STEM image of a single, cube-shaped $CsPbBr_3$ NC. Reprinted with permission from Ref. [40]. Copyright 2018, Springer Nature. (**d**) Photograph of $CsPbX_3$ NC dispersions under ultraviolet illumination. Reprinted with permission from Ref. [46]. Copyright 2015, American Chemical Society.

2.2. Synthesis

The controlled synthesis of high-quality MHP NCs is a prerequisite for exploring their self-assembly and collective optical behavior, for which precise control over size, morphology, and luminescent properties plays a decisive role. Several reliable liquid-phase synthetic routes have been accordingly developed [42,45–48,62,75,76]. Herein, we highlight two of the most prevalent methods: hot-injection (HI) [45,46] and ligand-assisted reprecipitation (LARP) [47,48]. After outlining their basic approaches, we discuss the key parameters that regulate NC size and shape. The resulting well-defined NCs act as ideal modular units, providing a solid material platform for the design and construction of SLs.

2.2.1. HI

The HI method is currently the most widely employed approach due to its ability to produce high-quality NCs with excellent reproducibility [46,77]. In this approach, one precursor is rapidly injected into a hot solution containing the remaining precursors, ligands, and a high-boiling-point solvent. This instantaneous mixing generates a transient high supersaturation, triggering rapid nucleation, which is subsequently followed by crystal growth [45,78]. The reaction is then quenched in an ice bath to halt further growth, resulting in NCs with a narrow size distribution (Figure 2a) [64]. In 2015, Protesescu et al. first applied this approach to synthesize $CsPbX_3$ NCs, which displayed well-defined cubic morphology and crystal structure alongside outstanding optical properties [46]. This seminal work drew significant attention from the research community and spurred rapid advances in the field.

Building on this foundation, numerous studies have focused on exploring the morphology control of halide PNCs [44,46,75–77,79–85]. Through careful adjustment of key parameters, such as reaction temperature [46,77], precursor [80,84,86], ligands [78,80], and solvents [83], a variety of colloidal NCs with finely tuned sizes and shapes have been realized, including nanocubes, nanoplatelets (NPLs), nanowires (NWs), and rhombic dodecahedra, among others (Figure 2d) [46,76,79,82–84,87,88]. It is well established that high temperatures and prolonged reaction times generally lead to the formation of large cubic NCs, often accompanied by broad size distributions [46], whereas lower temperatures favor the formation of anisotropic NCs [77,80,83,89]. Another representative work was reported by Pan et al., who systematically varied the length of the hydrocarbon chains of carboxylic acids and amines to elucidate their independent effects on NC size and morphology. The study demonstrates that, despite weaker surface binding compared to carboxylates, ammonium ions are more efficient in shaping anisotropic NPLs, whereas stronger carboxylate ligands effectively regulate the size of more isotropic nanocubes. Under identical temperature conditions, shorter carbon chain carboxylic acids produce nanocubes with increasing edge dimensions (Figure 2e) [80]. These established synthetic protocols thus provide a robust and versatile materials platform for further exploration of their intrinsic properties and programmable assembly.

2.2.2. LARP

The LARP method is another widely used approach for synthesizing PNCs. In this method, precursors are dissolved in a polar solvent (e.g., N,N-dimethylformamide (DMF) or dimethyl sulfoxide (DMSO)) and subsequently introduced into a poor solvent (e.g., toluene or hexane) in the presence of ligands, generating instantaneous supersaturation that induces NC nucleation and growth (Figure 2b) [48,64,90]. Compared with HI, the LARP approach is simpler, can be performed under ambient conditions, and typically proceeds at room temperature [64,91]. Zhang et al. first applied this simple strategy in 2015 to prepare $CH_3NH_3PbX_3$ QDs [48]. Later, Sun et al. showed that the morphology of $CsPbX_3$ NCs could be controlled by selecting appropriate organic acid and amine ligands, producing spherical QDs, nanocubes, nanorods (NRs), and few-unit-cell-thick NPLs (Figure 2c) [47].

Owing to its ability to suppress vertical growth while promoting lateral extension via rapid supersaturation, low temperatures, and selective ligand adsorption, the LARP method is widely employed to fabricate two-dimensional (2D) NPLs [47,62,90,91]. For instance, varying the ratio of monovalent to divalent cations and the amount of acetone can effectively control lateral growth [90], while the addition of extra HBr allows protonated oleylamine (OLA) to compete with Cs^+ ions on the NPL surface, slowing vertical growth and enabling fine adjustment of the final thickness [91]. These mature synthesis and precise control techniques provide a cornerstone for further investigations into the properties and assembly of these materials.

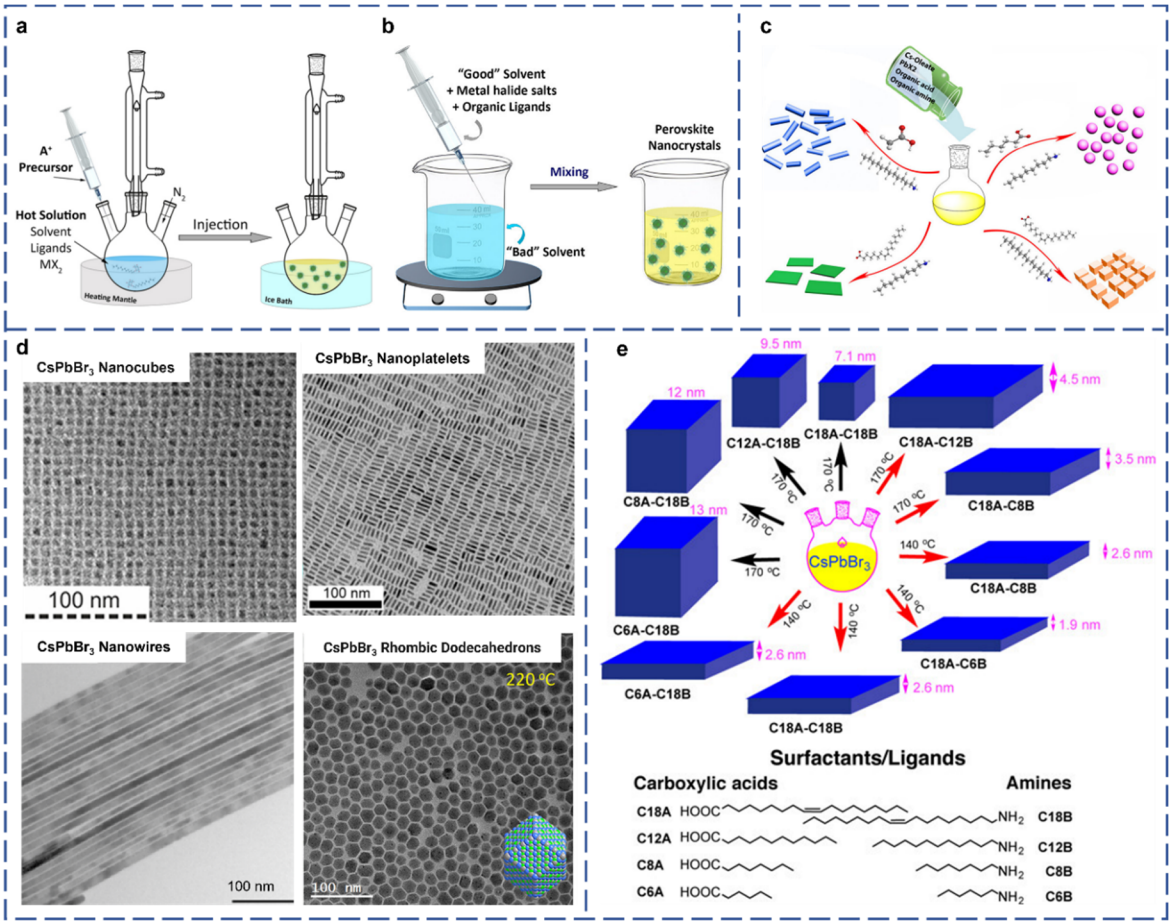

Figure 2. Synthesis of PNCs and Control of Their Morphology. Sketches of the (**a**) HI and (**b**) LARP methods used for the synthesis of colloidal MHP NCs. Reprinted with permission from Ref. [64]. Copyright 2019, American Chemical Society. (**c**) Room-temperature ligand-mediated synthesis of $CsPbX_3$ (X = Cl, Br, I) NCs with controlled morphologies: QDs, nanocubes, NRs, and ultrathin NPLs via different acid-amine ligand pairs. Reprinted with permission from Ref. [47]. Copyright 2016, American Chemical Society. (**d**) PNCs with different morphologies prepared by the HI method, including nanocubes, NPLs, NWs, and rhombic dodecahedra. Reprinted with permission from Refs. [46,79,83,84], respectively. Copyright 2015, 2019, 2015, and 2020, American Chemical Society. (**e**) Effect of carboxylic acid and amine chain length on NC shape and size. Reprinted with permission from Ref. [80]. Copyright 2016, American Chemical Society.

2.3. Surface Chemistry and Ligands

At the nanoscale, the extremely high surface-to-volume ratio renders surface properties the dominant factor governing the performance of PNCs [39,63,92–94]. For a more detailed account of the peculiarities of the surface chemistry of MHPs, we direct the reader to this review article [39]. This section focuses on elucidating how surface states and ligands serve as critical mediators of NC self-assembly, functioning not only to orchestrate inter-NC interactions and guide assembly pathways toward specific SL architectures but also to directly modulate optoelectronic coupling, collectively determining the macroscopic properties of the resulting SLs [68,95].

Specifically, regarding ligands, their binding to MHP NC surfaces is inherently dynamic (Figure 3a) [73], with coordination mode (monodentate [96], bidentate [27,30,97–100], or multidentate) fundamentally dictating binding strength and kinetic stability (Figure 3c) [101,102]. Bidentate or multidentate ligands typically induce strong chelation, leading to robust ionic bonding and efficient defect passivation. In contrast, traditional long-chain monodentate ligands such as OLA exhibit weaker, more dynamic binding, high mobility, and a propensity to desorb during purification or post-processing, often resulting in the re-emergence of surface trap states [103].

Beyond coordination strength, ligands maintain colloidal stability through steric or electrostatic effects. Steric stabilization originates from osmotic pressure generated by solvent exclusion within the ligand corona as NCs approach, which, combined with steric repulsion, prevents aggregation. Electrostatic stabilization allows ligands, acting as electron donors or acceptors, to tune surface potential and charge distribution; functionalization of alkyl chain termini can further introduce charge, enhancing electrostatic repulsion. These two mechanisms underpin stable colloidal dispersion [63,98].

Under controlled conditions, these stable colloidal dispersions can guide the transition from disordered NCs to ordered SLs. The assembly process relies predominantly on weak, ligand-mediated interactions, such as electrostatic forces, hydrogen bonding, and π-π stacking, rather than on the NC cores alone [104,105]. Ligand length, rigidity, and functionalization jointly tune the enthalpy-entropy balance of assembly: while shorter ligands [33,106] reduce interparticle spacing and enhance optoelectronic coupling, they may compromise colloidal stability. Branched ligands [29,78,107–111], such as the widely used didodecyldimethylammonium bromide (DDAB) [112], balance this trade-off by providing sufficient steric repulsion to maintain stability while shortening interparticle distance (Figure 3b) [112]. As a result, DDAB has been widely employed in the self-assembly of MHP NCs [60]. Meanwhile, more rigid ligands, including those with aromatic moieties [113–115], can impose defined orientational constraints and stronger directional interactions via π-π stacking, thereby promoting the formation of highly ordered SL architectures [116].

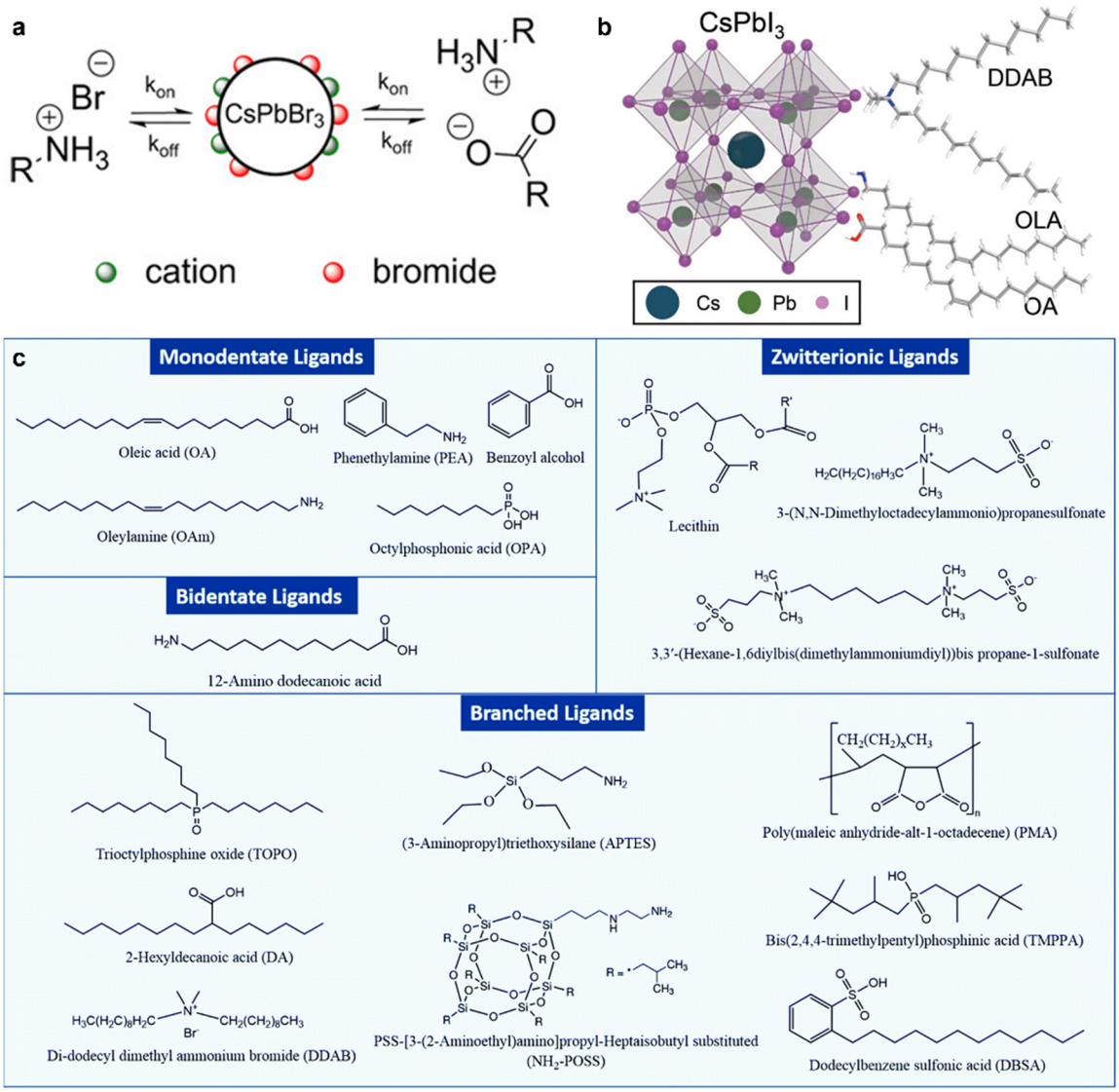

Figure 3. Surface Ligands in PNCs. (**a**) Highly dynamic ligand binding on PNC surfaces. Reprinted with permission from Ref. [73]. Copyright 2016, American Chemical Society. (**b**) Representative DDAB ligands used for self-assembly. Reprinted with permission from Ref. [112]. Copyright 2020, Royal Society of Chemistry. (**c**) Classification of ligands, including monodentate, bidentate, branched, and zwitterionic ligands. Reprinted with permission from Ref. [101]. Copyright 2021, Royal Society of Chemistry.

2.4. Post-Synthetic Treatment

PNCs obtained directly from synthesis usually require further refinement to achieve highly uniform size, well-defined surface chemistry, and desired functional properties. Implementing a controlled post-synthetic workflow [117] is therefore crucial. First, separation and purification steps are indispensable. These steps remove unreacted precursors, excess ligands, and aggregates, and through careful adjustment of centrifugation parameters

and solvent polarity [74,118], produce NCs with uniform size and morphology. A representative method involves stepwise antisolvent purification using ethyl acetate, whose moderate polarity selectively precipitates ligand-capped nanocrystals, enabling the isolation of specific nanostructures such as ultrathin NWs and increasing their purity from a few percent to over 90% [119]. Such strategies effectively narrow morphology and size distributions, providing a necessary foundation for the formation of long-range ordered SLs. Moreover, a cornerstone of post-synthetic treatment is ligand exchange, wherein native surface ligands are replaced with functional alternatives. By judiciously selecting ligands based on their functional groups, chain lengths, or synergistic combinations, researchers can effectively passivate surface defects [117], precisely fine-tune interparticle spacing and interactions during self-assembly, and therefore adjust the structure and the collective properties of the result SLs.

2.5. Optical Properties

MHP NCs serve as an ideal platform for investigating supermaterials, a role mainly attributable to their exceptional optical characteristics, in which collective behavior arises from the coupling of individual nanoscale units [118]. Understanding optical properties at the NC level is therefore essential for rationalizing the emergence of collective phenomena in SLs [35,67].

First, they exhibit benchmark performance metrics, including the extremely high PLQYs and narrow full widths at half-maximum (FWHMs) even without passivation, resulting from their direct bandgap, high carrier mobility, and defect tolerance [51–53,117]. In particular, PNCs display pronounced size- and composition-dependent bandgap and absorption characteristics. As the NC size decreases, quantum confinement [42–44] becomes increasingly significant, leading to a widening of the bandgap and a concomitant blue shift of the absorption edge. As a representative case of strong 2D confinement, NPLs exhibit a progressive blue shift of the optical bandgap with decreasing thickness (Figure 4a) [91]. Similarly, Protesescu et al. showed that adjusting the halide composition allows for continuous tuning of absorption and emission across the visible and near-infrared regions (Figure 4b) [46].

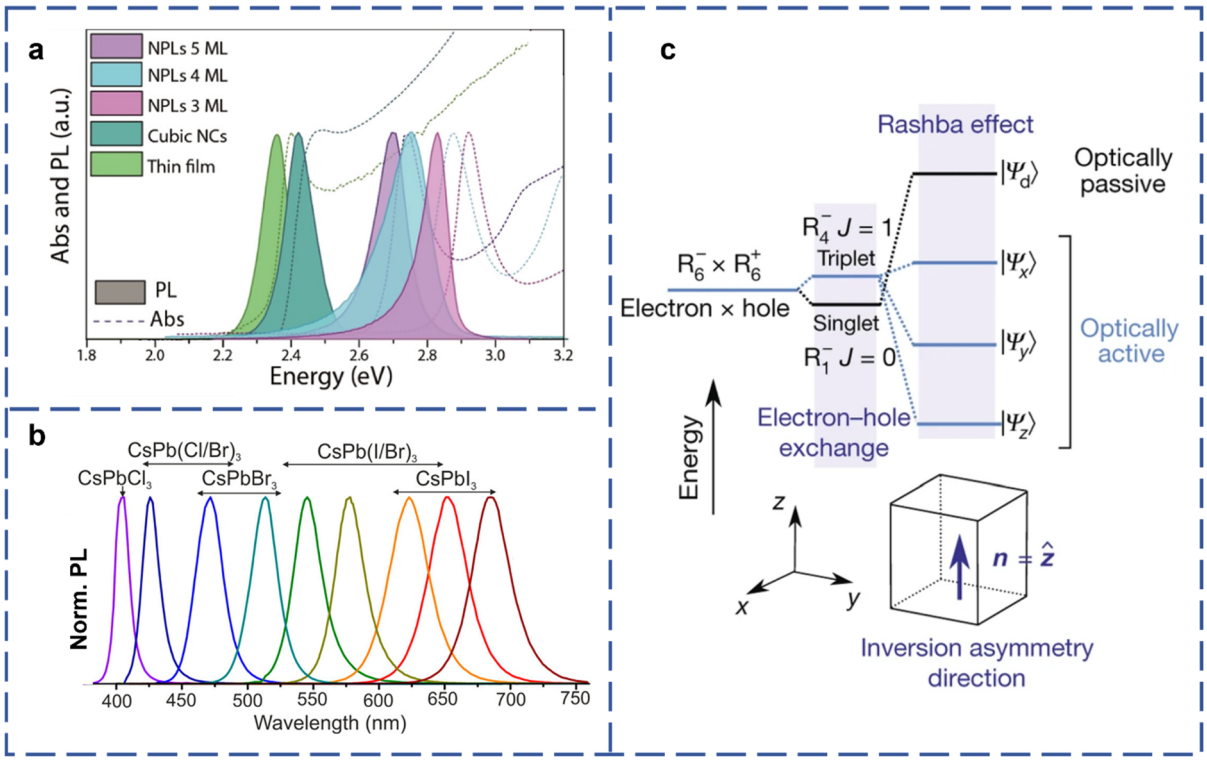

Figure 4. Optical Tunability and Triplet Excitons in PNCs. (**a**) Absorption and PL spectra of $CsPbBr_3$ thin films, nanocubes, and NPLs of varying thickness. Reprinted with permission from Ref. [91]. Copyright 2016, American Chemical Society. (**b**) PL spectra of $CsPbX_3$ NCs with different halide compositions. Reprinted with permission from Ref. [46]. Copyright 2015, American Chemical Society. (**c**) Band-edge exciton fine structure in $CsPbBr_3$: three bright states and one dark state shaped by exchange, Rashba effect, and lattice distortion. Reprinted with permission from Ref. [58]. Copyright 2018, Springer Nature.

The deep-rooted origin of these optical characteristics lies in their exceptional excitonic physics. PNCs possess excitons with high exciton binding energies and long coherence times. This was decisively confirmed by

Becker et al. in 2018, who observed bright triplet excitons in cesium lead halide perovskites exhibiting long lifetimes and suppressed dephasing-conditions enabling macroscopic coherent states (Figure 4c) [58]. These high-quality excitons thus constitute a versatile platform for exploring many-body quantum physics at the mesoscale. When NCs self-assemble into close-packed SLs, excitonic wavefunctions or electromagnetic fields from neighboring units can overlap, producing coherent coupling that manifests as collective quantum phenomena, including SF and coherent energy transport.

3. Formation of Perovskite SLs

The discussion of MHPs follows a research progression from the properties of the "building blocks" to the assembly process. Having clarified the key physicochemical attributes of PNCs as fundamental units, this chapter focuses on their self-assembly process and introduces the preparation methods as well as the structural diversity of the resulting SLs.

3.1. NC Self-Assembly

Self-assembly refers to the process in which dispersed particles spontaneously aggregate via weak interactions, ultimately forming an ordered packing structure (Figure 5a) [71,120–123]. Approximately three decades ago, the first 3D semiconductor QD SLs were realized through the solvent-evaporation-induced self-assembly of monodisperse CdSe NCs, marking the inception of colloidal semiconductor SL research [124]. In general, the self-assembly process evolves through sequential stages: initial steric repulsion maintains the dispersed state; by modulating ligands or solvent environments, the repulsion can be attenuated, allowing aggregation; eventually, a thermodynamically stable SL structure forms in the dried state [95]. If the process destabilizes too rapidly, disordered aggregates result, whereas under near-equilibrium conditions with sufficiently slow progression, NCs can undergo adequate structural adjustments to form ordered polyhedral SLs (Figure 5a,b) [95].

Assembly is thermodynamically governed by free energy (F) minimization. The driving force for ordering is encapsulated in $\Delta F = \Delta U - T\Delta S$, with ΔU arising from interparticle interactions [70,71] and ΔS encompassing entropy contributions from particle degrees of freedom and ligand-mediated effects [125]. A grasp of these factors is essential for controlling assembly and achieving target supermaterials.

Therefore, this section is structured to first present a systematic discussion of key NC interactions, then address the principle of entropy maximization and representative packing models, thereby constructing an integrated foundation for the thermodynamics and structural ordering in self-assembly.

3.1.1. NC Interactions

van der Waals (*vdW*) Interactions

vdW interactions are fundamental forces between NCs, characterized as short-range interactions whose strength increases markedly with decreasing interparticle distance (Figure 5c) [72]. *vdW* interactions can be quantitatively described by the classical formula

$$U_{vdW}(r) = -\frac{C_{vdW}}{r^6} \quad (1)$$

where r is the interparticle spacing, and C_{vdW} is a material-dependent constant related to composition and polarizability [72]. Based on molecular polarity, *vdW* forces are categorized into three types: orientation forces (permanent dipole-dipole interactions between polar molecules), induction forces (resulting from polarization induced by permanent dipoles in neighboring molecules), and dispersion forces (arising from instantaneous dipole fluctuations) [70,71].

In MHP NCs, dipole-dipole interactions are widely regarded as one of the key drivers of self-assembly [126–128]. They offer clear directionality and can be flexibly adjusted by modifying NC composition, shape, surface ligands, and solvent environment. Their synergistic role in multi-body interactions further makes them a key mechanism for regulating SL symmetry, optical properties, and functional characteristics [127]. For instance, the one-dimensional (1D) $CsPbBr_3$ SL chains reported by Ji et al. were primarily driven by dipole-dipole interactions, with their ordered alignment facilitated by directionally interactive, anisotropically structured templates formed synchronously in solution [126].

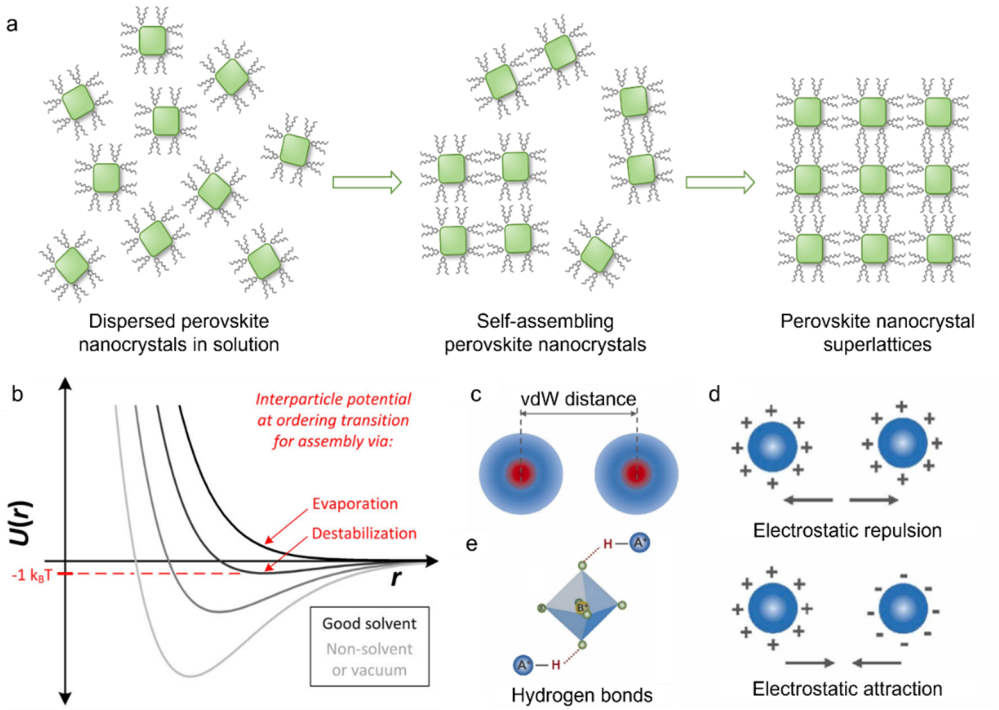

Figure 5. NC Self-Assembly. (**a**) Visualizing self-assembly: from dispersed NCs to ordered structures. Adapted with permission from Ref. [71]. Copyright 2024, Elsevier B.V. (**b**) Evolution of the effective pair interaction potential (U) with interparticle distance (r) during NC self-assembly, from the dispersed (darkest line) to the close-packed state (lightest line). Reprinted with permission from Ref. [95]. Copyright 2016, American Chemical Society. Key interactions in self-assembly: (**c**) *vdW* interactions, (**d**) electrostatic interactions, and (**e**) hydrogen bonding. Reprinted with permission from Ref. [72]. Copyright 2025, Elsevier B.V.

Electrostatic Interactions

Electrostatic interactions are prevalent among charged NCs. By modulating the composition of the MHPs and the ligands, the surface potential of the NCs can be altered, leading to either electrostatic repulsion or attraction between them (Figure 5d) [72]. The solvent environment plays a pivotal role in this regulation. Through dielectric screening, ion solvation, and the restructuring of the electrical double layer, it fine-tunes the strength, range, and direction of the electrostatic interactions, thereby governing colloidal stability and self-assembly pathways. To date, only a limited number of studies in the perovskite field have addressed this topic [120,129]. We contend that this is largely due to the ionic crystal nature of the material, the highly dynamic binding of ligands, and the facile migration of halide ions. These factors collectively make it challenging to establish a stable and controllable surface charge distribution, thus preventing electrostatic interactions from serving as an independent, stable, and precise dominant driving force within this system.

Hydrogen Bonding

Hydrogen bonding is a directional interaction formed between a hydrogen-bond donor (an X-H group bonded to a highly electronegative atom) and a hydrogen-bond acceptor (an electronegative atom with lone-pair electrons, such as N, O, or F) (Figure 5e) [72]. This type of interaction has been extensively studied in DNA-mediated self-assembly [130–132]. In MHP NCs, hydrogen bonds are typically introduced via surface ligands or polymeric functional groups, enabling the formation of inter-NC hydrogen-bonding networks that regulate orientational ordering, self-assembly pathways, and the formation of superstructures [88,133].

3.1.2. Entropy Maximization and Dense Packings

NC self-assembly involves a complex combination of factors such as interaction potentials, ligand configurations, and solvent effects. To isolate and understand the contribution of entropy, a hard-sphere model is commonly employed. In a good solvent, ligands are treated as fully extended, and NCs are primarily subject to steric repulsion that prevents overlap, with other energy contributions neglected (Figure 6a) [95]. Within this model, the free energy is purely entropy-driven. This leads to a counterintuitive insight: although crystalline structures appear highly ordered, their total entropy can exceed that of a disordered fluid. While collective ordering

of particle positions reduces configurational entropy, the additional free volume available for local vibrations and rotational motions near lattice positions increases translational and rotational entropy, which more than compensates for the configurational loss (Figure 6b–d) [95,134], making the crystalline phase thermodynamically favorable.

In predicting NC self-assembly, dense packing is generally considered the most likely configuration, most commonly realized as face-centered cubic (fcc) or hexagonal close-packed (hcp) arrangements. By contrast, alternative candidate structures such as body-centered cubic (bcc), simple hexagonal, and simple cubic packings exhibit lower packing densities of 68%, 60%, and 52%, respectively (Figure 6e) [95], resulting in larger voids within the lattice and correspondingly reduced thermodynamic stability. For NCs with a cubic shape, the most common morphology in MHP NCs, 3D dense packings typically result in so-called "supercubes" (Figure 6f,g) [67,135]. In these structures, the individual cubic NCs align face-to-face, forming ordered SLs with minimal void space.

3.1.3. Packing Models

Based on the hard-sphere assumption, the optimal packing model (OPM) was first proposed to predict the packing motifs of NC SLs. In this model, NCs are idealized as rigid units, while ligand shells are assumed to fill space solely along the interparticle center-to-center direction (Figure 6h) [136]. Such assumptions allow OPM to successfully describe simple SLs, particularly in short-ligand systems.

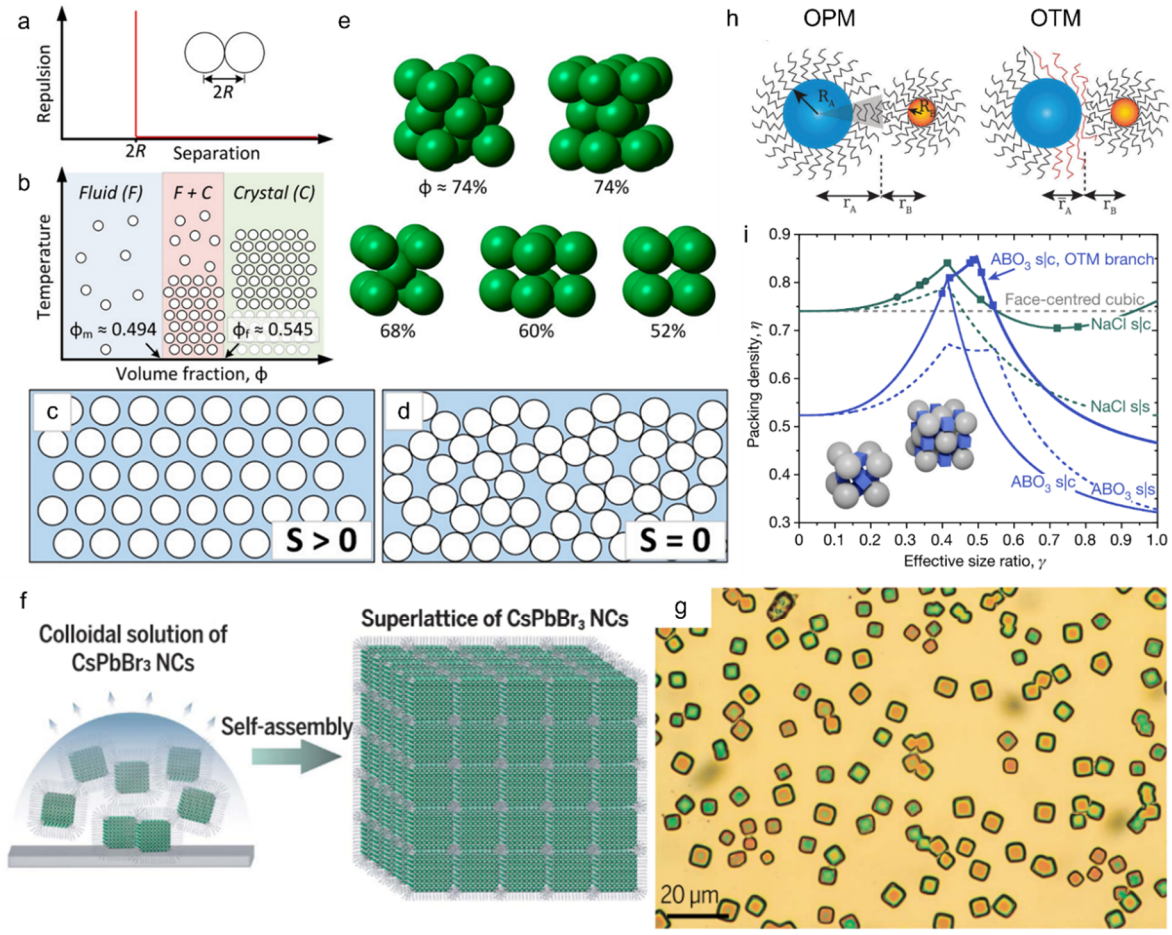

Figure 6. Packing Principles in NC Self-Assembly. (**a**) Hard-sphere interaction potential. (**b**) Phase diagram of noninteracting spheres, showing fluid, crystalline, and coexistence regions. (**c**,**d**) Compared with jammed disordered states, the transition to an ordered colloidal crystal increases the accessible free volume per particle, leading to a significant increase in configurational entropy. (**e**) Representative dense and less-dense sphere packings, including fcc, hcp, bcc, simple hexagonal, and simple cubic structures. Reprinted with permission from Ref. [95]. Copyright 2016, American Chemical Society. (**f**) Self-assembly of $CsPbBr_3$ NCs into a supercube. (**g**) Optical microscopy image of large supercubes. Reprinted with permission from Ref. [67]. Copyright 2017, American Association for the Advancement of Science. (**h**) Schematics of the OPM and the OTM. Reprinted with permission from Ref. [136]. Copyright 2017, Royal Society of Chemistry. (**i**) Packing-density-predicted binary ABO_3-type (blue) and NaCl-type (green) SLs, with solid and dashed lines denoting s|c and s|s binary mixtures, respectively; symbols indicate experimentally observed $CsPbBr_3$ SLs. Reprinted with permission from Ref. [60]. Copyright 2021, Springer Nature.

In practice, however, NCs exhibit pronounced softness arising from a combination of interparticle and ligand-mediated interactions, leading to systematic deviations from OPM predictions. To address these limitations, the orbifold topological model (OTM) was introduced to explicitly incorporate ligand deformability and topological constraints on ligand conformations (Figure 6h) [136–138]. As demonstrated by Cherniukh et al., in binary perovskite SLs assembled from lead halide perovskite nanocubes, OPM is valid only at small size ratios ($\gamma \leq 0.414$), whereas at larger size ratios, OTM captures shape-induced orientation locking and ligand-mediated topological effects, enabling packing densities far exceeding those predicted by hard-sphere models and stabilizing complex SL architectures (Figure 6i) [60].

Complementary insights were provided by Boles and Talapin, who showed that in 2D assemblies, OPM accurately predicts experimental structures only at sufficiently high coordination numbers [139]. For low-coordination motifs, the overlap cone model (OCM) [139,140] was proposed, in which ligand shells are allowed to overlap, resulting in reduced equilibrium interparticle separations. OCM has proven effective in describing low-coordination SLs, including CsCl- and CaB_6-type structures [139,140].

3.2. Controllable Formation and Structural Diversity of Perovskite SLs

3.2.1. Assembly Pathways toward Ordered SLs

Ordered colloidal NC SLs [141] are typically constructed by solvent evaporation or colloidal destabilization [142–145], which brings NCs into close proximity and drives self-assembly. For MHP NCs, various assembly strategies have been developed [143], among which solvent evaporation is the most widely used due to its simplicity and broad applicability. A typical protocol involves drop-casting a small volume of dilute NC solution onto a substrate and allowing natural drying (Figure 7a) [95]. For instance, Rainò and colleagues deposited 10 μL of a $CsPbBr_3$ NC dispersion in toluene onto a substrate and allowed the solvent to evaporate slowly, resulting in the formation of micron-sized 3D SLs (Figure 7c) [118] and the observation of SF. Another controllable strategy is to perform evaporation in a small vial with the substrate placed at a tilt, enabling regulation of meniscus movement (Figure 7a) [95]. Cherniukh et al. employed 28–35 μL of a NC mixture in a tilted vial containing a substrate and carried out evaporation at 0.45 atm and room temperature, producing slowly evaporated, thermodynamically stable complex SL phases in multicomponent systems (Figure 7d,e) [60]. In these methods, solvent properties, external pressure, and temperature are critical parameters, as they govern evaporation and assembly kinetics, profoundly affecting the structural order. Typically, low temperature and ambient or low-vacuum conditions favor slow, well-ordered assembly, whereas rapid evaporation can lead to disorder.

Beyond evaporation, alternative strategies such as ultrasonication, template-assisted assembly, and liquid-air interface assembly have also been explored. Tong et al. showed that probe-tip ultrasonication of $CsPbBr_3$ NCs produces individual dispersed NCs at low precursor concentration and spontaneously forms self-assembled superstructures at higher concentrations (Figure 7b) [146].

3.2.2. Structural Diversity in Perovskite SLs

Building upon a deep understanding of the controllable synthesis and self-assembly principles of PNCs, researchers have successfully created a diverse range of PNC SLs. This section aims to systematically introduce the structural diversity [126,128,147,148] of these SLs based on their composition and dimensionality.

Within single-component SLs, in addition to the classic 3D cubic packing (Figure 7c) [118], Pan and colleagues reported a 1D chain-like structure formed by NCs inside semi-cylindrical $PbSO_4$ "pods", illustrating the balance between component solvophilicity and solvophobicity [149]. By further reducing NC size, studies have advanced from achieving single-string "pearl necklace" type 1D assemblies to developing 2D $CsPbBr_3$ NC SLs featuring two or three rows of close-packed structures [149]. For 2D architectures, NPLs serve as essential building blocks [150,151]. Ye and coworkers selected solvents with different boiling points and vapor pressures to regulate the evaporation kinetics, resulting in thin films with distinct NPL orientations on the substrate (Figure 7f) [152]. Slow-evaporating heptane induced a face-down arrangement, whereas fast-evaporating hexane led to an edge-up arrangement, demonstrating controlled orientation in 2D NPL SLs [152]. Another noteworthy 2D structure is the moiré SL [153–159], exemplified by the renowned magic-angle graphene [160]. Zhang et al., utilizing ultrathin, ligand-free halide perovskites and modulating ionic interactions, constructed square moiré patterns with tunable periods (Figure 7g) [154]. High-resolution transmission electron microscopy (HRTEM) directly visualized moiré structures with different periodicities (Figure 7h,i) and revealed the emergence of localized bright excitons and trapped charge carriers at a twist angle of approximately 10° [154].

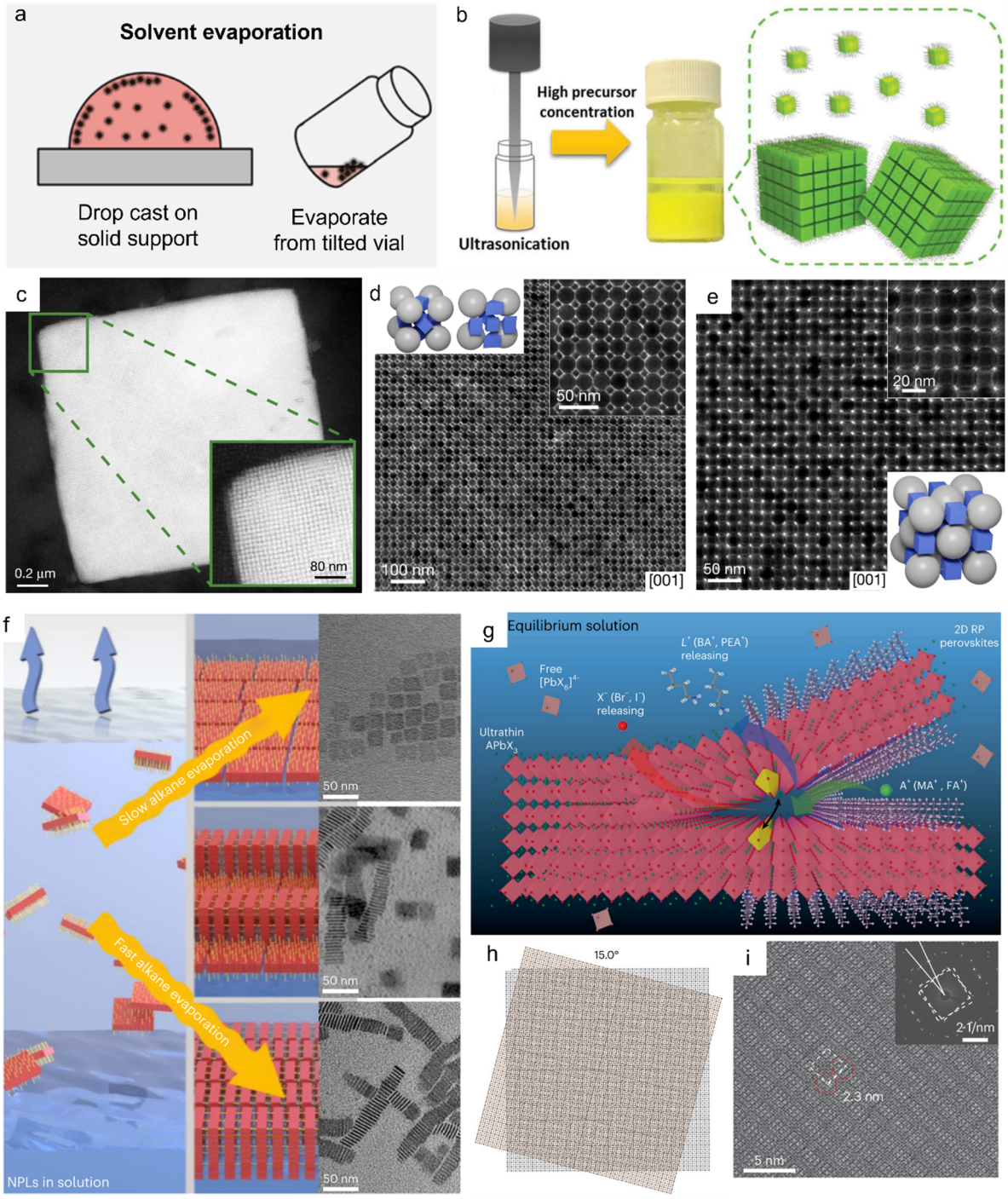

Figure 7. Formation Strategies and Structural Diversity of Perovskite SLs. (**a**) SL assembly via solvent evaporation. Reprinted with permission from Ref. [95]. Copyright 2016, American Chemical Society. (**b**) Single-step tip-sonication synthesis of $CsPbBr_3$ NCs: supercrystal formation at high concentration. Reprinted with permission from Ref. [146]. Copyright 2018, Wiley-VCH. (**c**) HAADF-STEM image of a $CsPbBr_3$ NC SL with simple cubic packing. Reprinted with permission from Ref. [118]. Copyright 2018, Springer Nature. (**d**) Binary ABO_3-type SLs assembled from $CsPbBr_3$ (8.6 nm) and Fe_3O_4 (19.5 nm) NCs, viewed along [001]. (**e**) Binary NaCl-type SLs formed from $CsPbBr_3$ (8.6 nm) and Fe_3O_4 (19.8 nm) NCs. Reprinted with permission from Ref. [60]. Copyright 2021, Springer Nature. (**f**) Orientation control of self-assembled $CsPbI_3$ NPLs. Reprinted with permission from Ref. [152]. Copyright 2024, Springer Nature. (**g**) Conversion of few-layer Ruddlesden-Popper (RP) perovskites to ultrathin $APbX_3$ in equilibrium solution. (**h**) Square moiré patterns in twisted $MAPbX_3$ bilayers (15.0°). (**i**) HRTEM image of 15.0°-twisted $MAPbBr_3$ bilayer NPLs. Reprinted with permission from Ref. [154]. Copyright 2024, Springer Nature.

In the realm of multi-component systems, Cherniukh and collaborators fabricated ABO_3-type binary and ternary perovskite SLs through shape-directed co-assembly [60]. This involves highly luminescent cubic $CsPbBr_3$ NCs occupying B/O lattice sites, spherical Fe_3O_4 or $NaGdF_4$ NCs occupying A sites, and truncated-cuboid PbS NCs occupying B sites (Figure 7d) [60]. Additionally, binary SL structures such as NaCl-type, AlB_2-type, and CuAu-type have been the subject of substantial research [60,161–163].

These SLs, built from NCs of varying types and sizes, essentially form functional metamaterials based on "artificial atoms". Their structural designs show potential to transcend the confines of traditional crystallographic systems, expanding the conceptual framework for material construction [57,142,164]. Furthermore, this rich structural diversity opens up a broad research landscape for delving into the novel characteristics of SLs, spanning properties [143,165,166], quantum behaviors [167–169], and collective physicochemical phenomena.

4. Collective Optoelectronic Effects in PNC SLs

Collective emission in a coherently coupled ensemble can differ drastically from single-emitter behavior [118,127,170,171]. MHP NC SLs are particularly suited for studying such collective optical phenomena because their bright triplet excitons possess high oscillator strength [58], slow dephasing, and minimal spectral inhomogeneity [2,59]. These characteristics render individual NCs strong optical dipoles, thereby enhancing coherent exciton-photon and exciton-exciton coupling, lowering the threshold for the onset of collective emission, and supporting long-lived collective coherence with negligible inhomogeneous broadening [2,58,59].

SF [170,171] is a collective quantum phenomenon, where an ensemble of initially uncorrelated excited emitters spontaneously synchronize through a shared optical field and evolve into a coherent quantum state (Figure 8a) [118]. This state gives rise to powerful cooperative emission, causing the emitters to radiate nearly simultaneously in an intense, ultrafast burst of light, followed by rapid decay [118,170,172]. In 2018, Rainò et al. reported SF in $CsPbBr_3$ SLs, with PL spectra showing a high-energy peak from uncoupled NCs and a narrow, red-shifted peak from coupled NCs (Figure 8b) [118]. At high excitation, radiative decay accelerates significantly (Figure 8c) [118], depending on excitation power, and the first-order coherence time increases over fourfold (Figure 8d) [118], confirming strong coherence [118].

SF is characterized by accelerated decay with increasing coupled emitter number N, a build-up time τD for achieving phase synchronization, and Burnham-Chiao ringing, where the emitted intensity oscillates due to emitter-light interactions (Figure 8e,f) [118]. These phenomena not only reveal the unique quantum cooperative behavior in NC SLs but also offer promising avenues for ultrafast light sources, high-brightness LEDs, and quantum photonic devices.

In contrast to the well-established collective optical behavior of PNC SLs, the mechanisms governing exciton and energy transport [173,174] remain poorly understood. Several hypotheses [69,175] persist regarding transport modes within such SLs. Research indicates that when the inter-NC distance is sufficiently small and the electronic coupling energy equals or exceeds the exciton binding energy, carrier transport may proceed primarily through tunneling. Conversely, when the coupling energy is lower, Förster resonance energy transfer (FRET) [41,94,121,176] dominates exciton energy transfer (Figure 8g) [177]. Notably, energy-transfer efficiency decreases significantly as the inter-NC spacing increases. Penzo et al. demonstrated that in highly ordered, closely packed $CsPbBr_3$ NC SLs, FRET serves as the primary energy-transfer mechanism and substantially enhances exciton diffusion between adjacent NCs (Figure 8h), leading to an exciton diffusion length of up to 200 nm. In contrast, in monodisperse yet disordered NC systems, the larger inter-NC spacing (≥20 nm) significantly suppresses FRET (Figure 8i) [177]. Similarly, using an ABO_6-type SL as a model system, Sekh et al. observed efficient inter-NC coupling and Förster-like energy transfer from strongly confined 5.3 nm $CsPbBr_3$ NCs to weakly confined 17.6 nm $CsPbBr_3$ NCs, accompanied by characteristic SF at low temperatures [161].

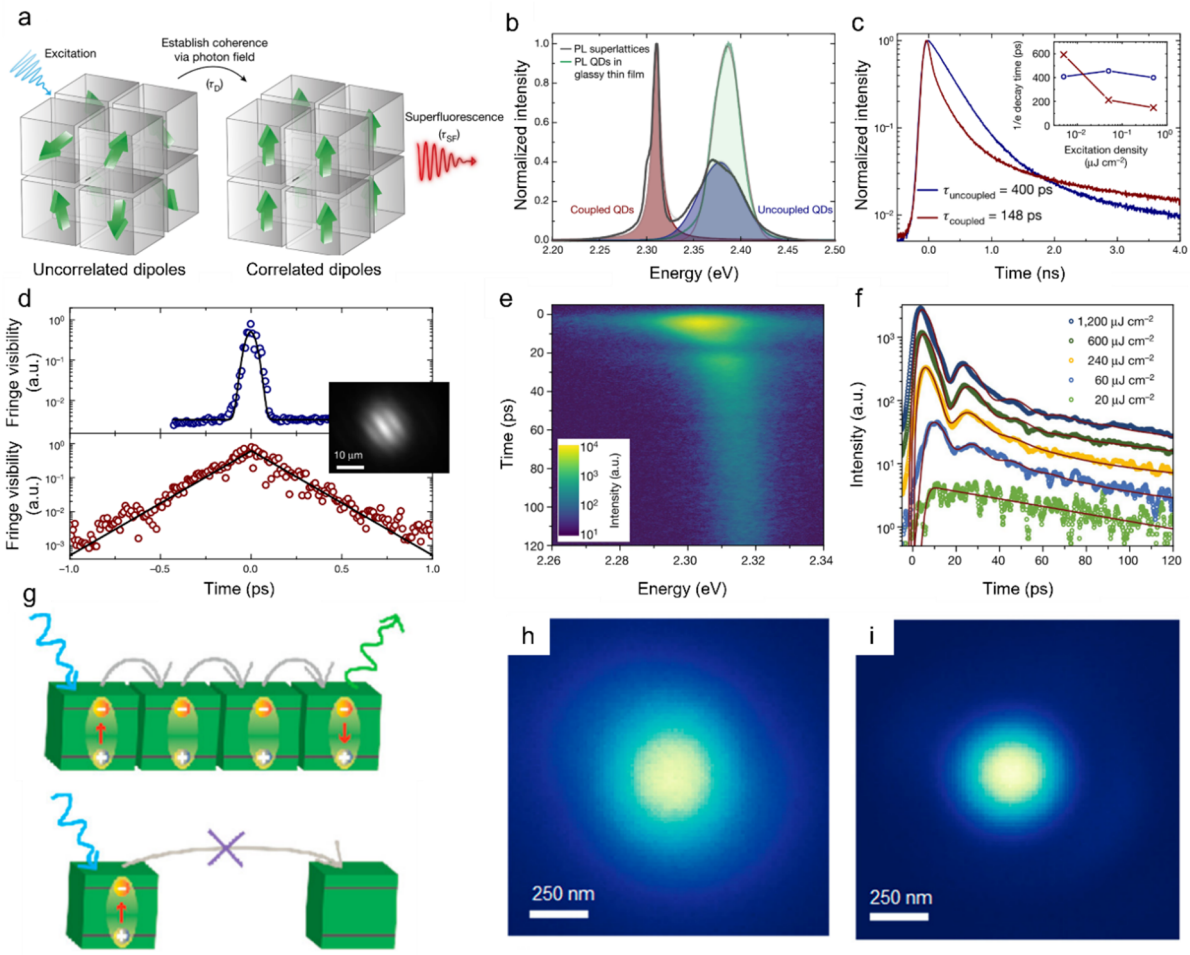

Figure 8. Collective Emission and FRET in Perovskite SLs. (**a**) Schematic of the SF build-up process. (**b**) PL spectrum of a single $CsPbBr_3$ SL. (**c**) TRPL decays of the two emission bands at 500 nJ cm^{-2}, with faster decay observed for coupled QDs. (**d**) First-order correlation functions of the two emission bands measured by a Michelson interferometer. (**e**) Streak-camera image of SF dynamics at 600 μJ cm^{-2}. (**f**) Time-resolved emission traces at different excitation powers with biexponential fits including damped oscillations. Reprinted with permission from Ref. [118]. Copyright 2018, Springer Nature. (**g**) Schematic of FRET-mediated exciton diffusion in close-packed and sparse PNC monolayers. (**h**,**i**) Normalized PL intensity profiles of close-packed (**h**) and sparse (**i**) PNC monolayers under 450 nm excitation. Reprinted with permission from Ref. [177]. Copyright 2024, American Chemical Society.

5. Applications

Despite the excellent optoelectronic properties of MHP SLs, their practical applications remain in the early stages, with most studies focusing on LEDs [71,72,152,178–180]. Kumar et al. demonstrated that anisotropic PNCs can be directed to self-assemble into SLs with the same orientation, effectively promoting horizontal transition dipole orientation and enhancing light outcoupling efficiency in LEDs (Figure 9a) [178]. Another significant advancement comes from the work of Ye et al., who developed LEDs from $CsPbI_3$ perovskite NPL SLs that emit highly linearly polarized light (74.4% polarization degree). This was achieved by controlling the self-assembly orientation to align transition dipoles, coupled with strong quantum/dielectric confinement and uniform NPL alignment inducing large excitonic fine-structure splitting (Figure 9b,c) [152]. This approach offers a tunable, solution-processable platform for advanced 3D displays and optical communication without complex optics.

Moving forward, intentionally designing diverse SL structures and controlling their macroscopic patterning for integration will allow researchers to venture beyond conventional optoelectronics. This paves the way for exploring complex many-body light-matter interactions in artificial quantum lattices, potentially leading to breakthroughs such as ultra-bright coherent assemblies or practical, scalable sources of entangled photons for optical quantum computing and quantum imaging. MHP SLs thus stand at the threshold of evolving from high-performance materials into functional quantum architectures [60].

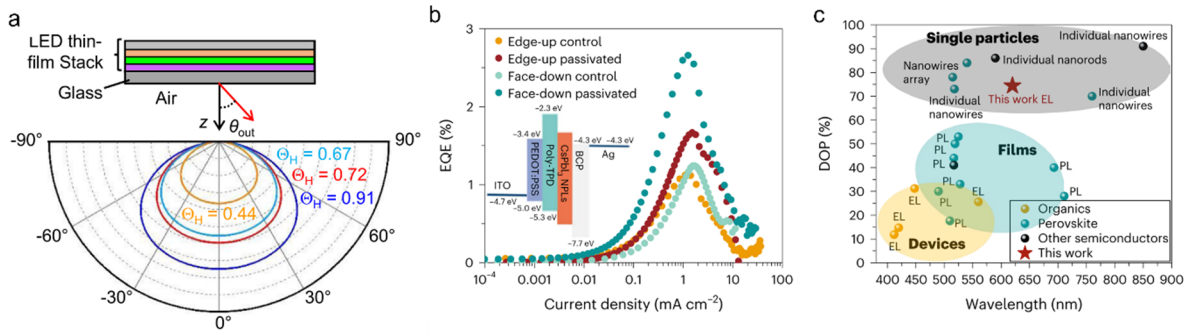

Figure 9. Applications of MHP SLs. (**a**) Calculated far-field emission patterns (FEPs) of the emitting layers (EMLs) in the optimized LED stack at different Θ_H values, showing enhanced radiation power outcoupled to air with increasing Θ_H. Reprinted with permission from Ref. [178]. Copyright 2020, Springer Nature. (**b**) Current density versus external quantum efficiency (EQE) for pristine and passivated edge-up and face-down NC plate LEDs. Inset: optimized LED device structure. (**c**) Comparison of the degree of polarization (DOP) for different materials at the single-particle, thin-film, and device levels. Reprinted with permission from Ref. [152]. Copyright 2024, Springer Nature.

6. Outlook

In recent years, following the discovery of collective emission in MHP NC SLs [118], increasing attention has been devoted to MHP NCs and SLs [118,147,152]. The field has expanded rapidly, driven by the synthetic accessibility of PNCs, advances in self-assembly engineering, and progressively deeper mechanistic insights into their photophysical behavior. Despite this remarkable progress, several critical challenges remain unresolved. In the following discussion, we delineate these open questions and discuss their broader implications.

As the fundamental building blocks of self-assembled SLs, PNCs face significant stability challenges, as they are prone to degradation under light, moisture, and heat [49,63]. This inherent instability not only promotes undesirable aggregation during self-assembly, limiting structural reproducibility, but also hinders practical applications. Besides, in multicomponent systems, ion migration further complicates the landscape by disrupting local composition and lattice integrity, thereby compromising structural diversity and optical performance. Strategies such as surface ligand modification, doping, and the integration of low-dimensional NCs have shown promise in addressing these issues. However, achieving durable, high-performance SLs remains an ongoing pursuit. Beyond these challenges, the capability for multidimensional modulation at the nanoscale facilitates the creation of new SL architectures [57,181–187] and the emergence of properties [188–194] absent in conventional atomic crystals, thereby opening broader possibilities for multifunctional SLs [130–132,195–197]. For example, the concept of patchy surface NCs provides an innovative design strategy for NCs as building blocks [198]. By enabling directional interparticle interactions and customizable surface functionalities, patchy PNCs greatly expand the possibilities for constructing SLs with precisely controlled architectures and novel properties.

The prevailing design of SLs has largely focused on studying, imitating, and extending conventional atomic crystals [199–202]. Research on MHP NC SLs remains at an early stage, with initial control over composition and simple crystalline symmetries [60,153,154,161–163,203]. However, exploration of more complex lattice types, such as non-close-packed or open-framework structures, remains limited. For instance, in other colloidal nanocrystal systems, strategies such as incorporating liquid crystal molecules to form colloidal interstitial solid solutions with ultralarge thermal expansion [164] or using DNA strands to achieve directional non-close-packed architectures have been demonstrated [130]. These studies inspire new design concepts for PNC SLs, offering the potential to construct more diverse and multifunctional SL architectures.

Beyond structural diversity, another key frontier lies in harnessing the unique collective optical phenomena that can emerge from ordered NC assemblies. SF is among the most fascinating properties of MHP NCs, yet its signature becomes increasingly elusive at elevated temperatures. Even at cryogenic temperatures (e.g., 6 K), where SF intensity is relatively high, experimental signals still fall short of theoretical predictions by six orders of magnitude [204]. This discrepancy underscores a central challenge: suppressing the thermal disruption of coherent coupling to enable efficient SF at higher temperatures, a crucial hurdle that must be overcome for further progress in this field. Despite these challenges, efforts in material optimization, fabrication, and theory, together with surface passivation, precise self-assembly, cavity enhancement, and simulations, offer promise for overcoming them. Achieving efficient, stable SF would enable new applications in optoelectronics and quantum information processing.

Author Contributions

R.D. conceived the scope and structure of this review article and was responsible for the literature survey, analysis, and interpretation of the relevant studies, as well as writing the original draft and critically revising the manuscript for important intellectual content. J.W.L. provided helpful discussion. R.W. served as the corresponding author and provided overall supervision, conceptual guidance, and resources for this work, and contributed to the review and editing of the manuscript. All authors have read and agreed to the published version of the manuscript.

Funding

R.W. acknowledges financial support from the National Natural Science Foundation of China (Grant No. 62474143), the Key R&D Program of Zhejiang Province (2024SSYS0061), the Muyuan Laboratory (Program ID 14136022401), the Scientific Research Innovation Capability Support Project for Young Faculty (SRICSPYF-BS2025014), the Zhejiang Key Laboratory of Low-Carbon Intelligent Synthetic Biology (2024ZY01025), and the Natural Science Foundation of Zhejiang Province (Grant Nos. LD24E020001, LDG25E020001, and LD22E020002). J.-W.L. acknowledges the financial support by the Super-Gap Strategy Research Project by Korea Research Institute of Chemical Technology (KRICT, KS2522-30-03) and National Research Foundation of Korea (NRF) grant funded by the Korea government (MSIT, RS-2024-00404694).

Institutional Review Board Statement

Not applicable.

Informed Consent Statement

Not applicable.

Data Availability Statement

The data supporting this review article can be obtained from authors or references.

Conflicts of Interest

The authors declare no conflict of interest.

Use of AI and AI-Assisted Technologies

During the preparation of this work, the author used Large Language Models for spelling and grammar checks. After using this tool, the author reviewed and edited the content as needed and takes full responsibility for the content of the published article.

References

1. Liu, M.X.; Yazdani, N.; Yarema, M.; et al. Colloidal quantum dot electronics. *Nat. Electron.* **2021**, *4*, 548–558.
2. Utzat, H.; Sun, W.W.; Kaplan, A.E.K.; et al. Coherent single-photon emission from colloidal lead halide perovskite quantum dots. *Science* **2019**, *363*, 1068–1072.
3. Jung, H.S.; Park, N.G. Perovskite Solar Cells: From Materials to Devices. *Small* **2015**, *11*, 10–25.
4. Lee, M.M.; Teuscher, J.; Miyasaka, T.; et al. Efficient Hybrid Solar Cells Based on Meso-Superstructured Organometal Halide Perovskites. *Science* **2012**, *338*, 643–647.
5. Eperon, G.E.; Leijtens, T.; Bush, K.A.; et al. Perovskite-perovskite tandem photovoltaics with optimized band gaps. *Science* **2016**, *354*, 861–865.
6. Correa-Baena, J.; Saliba, M.; Buonassisi, T.; et al. Promises and challenges of perovskite solar cells. *Science* **2017**, *358*, 739–744.
7. Li, Z.; Klein, T.R.; Kim, D.H.; et al. Scalable fabrication of perovskite solar cells. *Nat. Rev. Mater.* **2018**, *3*, 18017.
8. Akkerman, Q.; Gandini, M.; Di Stasio, F.; et al. Strongly emissive perovskite nanocrystal inks for high-voltage solar cells. *Nat. Energy* **2017**, *2*, 16194.
9. Burschka, J.; Pellet, N.; Moon, S.-J.; et al. Sequential deposition as a route to high-performance perovskite-sensitized solar cells. *Nature* **2013**, *499*, 316–319.
10. Park, N.-G. Perovskite solar cells: An emerging photovoltaic technology. *Mater. Today* **2015**, *18*, 65–72.
11. Kim, J.Y.; Lee, J.-W.; Jung, H.S.; et al. High-Efficiency Perovskite Solar Cells. *Chem. Rev.* **2020**, *120*, 7867–7918.

12. Jena, A.K.; Kulkarni, A.; Miyasaka, T. Halide Perovskite Photovoltaics: Background, Status, and Future Prospects. *Chem. Rev.* **2019**, *119*, 3036–3103.
13. Zhang, J.; Wang, L.; Jiang, C.; et al. $CsPbBr_3$ Nanocrystal Induced Bilateral Interface Modification for Efficient Planar Perovskite Solar Cells. *Adv. Sci.* **2021**, *8*, 2102648.
14. Xue, J.; Wang, R.; Chen, L.; et al. A Small-Molecule "Charge Driver" enables Perovskite Quantum Dot Solar Cells with Efficiency Approaching 13%. *Adv. Mater.* **2019**, *31*, 1900111.
15. Xiao, Z.; Kerner, R.A.; Zhao, L.; et al. Efficient perovskite light-emitting diodes featuring nanometre-sized crystallites. *Nat. Photonics* **2017**, *11*, 108–115.
16. Chiba, T.; Hayashi, Y.; Ebe, H.; et al. Anion-exchange red perovskite quantum dots with ammonium iodine salts for highly efficient light-emitting devices. *Nat. Photonics* **2018**, *12*, 681–687.
17. Yuan, M.; Quan, L.N.; Comin, R.; et al. Perovskite energy funnels for efficient light-emitting diodes. *Nat. Nanotechnol.* **2016**, *11*, 872–877.
18. Tan, Z.-K.; Moghaddam, R.S.; Lai, M.L.; et al. Bright light-emitting diodes based on organometal halide perovskite. *Nat. Nanotechnol.* **2014**, *9*, 687–692.
19. Stranks, S.D.; Snaith, H.J. Metal-halide perovskites for photovoltaic and light-emitting devices. *Nat. Nanotechnol.* **2015**, *10*, 391–402.
20. Liu, X.-K.; Xu, W.; Bai, S.; et al. Metal halide perovskites for light-emitting diodes. *Nat. Mater.* **2020**, *20*, 10–21.
21. Fakharuddin, A.; Gangishetty, M.K.; Abdi-Jalebi, M.; et al. Perovskite light-emitting diodes. *Nat. Electron.* **2022**, *5*, 203–216.
22. Li, H.; Zhu, X.; Zhang, D.; et al. Thermal management towards ultra-bright and stable perovskite nanocrystal-based pure red light-emitting diodes. *Nat. Commun.* **2024**, *15*, 6561.
23. Chu, Z.M.; Zhao, Y.; Ma, F.; et al. Large cation ethylammonium incorporated perovskite for efficient and spectra stable blue light-emitting diodes. *Nat. Commun.* **2020**, *11*, 4165.
24. Ma, D.; Lin, K.; Dong, Y.; et al. Distribution control enables efficient reduced-dimensional perovskite LEDs. *Nature* **2021**, *599*, 594–598.
25. Lin, K.; Xing, J.; Quan, L.N.; et al. Perovskite light-emitting diodes with external quantum efficiency exceeding 20 per cent. *Nature* **2018**, *562*, 245–248.
26. Kim, J.S.; Heo, J.-M.; Park, G.-S.; et al. Ultra-bright, efficient and stable perovskite light-emitting diodes. *Nature* **2022**, *611*, 688–694.
27. Hassan, Y.; Park, J.; Crawford, M.; et al. Ligand-engineered bandgap stability in mixed-halide perovskite LEDs. *Nature* **2021**, *591*, 72–77.
28. Cao, Y.; Wang, N.; Tian, H.; et al. Perovskite light-emitting diodes based on spontaneously formed submicrometre-scale structures. *Nature* **2018**, *562*, 249–253.
29. Yang, J.; Chen, T.; Ge, J.; et al. High Color Purity and Efficient Green Light-Emitting Diode Using Perovskite Nanocrystals with the Size Overly Exceeding Bohr Exciton Diameter. *J. Am. Chem. Soc.* **2021**, *143*, 19928–19937.
30. Pan, J.; Shang, Y.; Yin, J.; et al. Bidentate Ligand-Passivated $CsPbI_3$ Perovskite Nanocrystals for Stable Near-Unity Photoluminescence Quantum Yield and Efficient Red Light-Emitting Diodes. *J. Am. Chem. Soc.* **2017**, *140*, 562–565.
31. Liu, M.; Wan, Q.; Wang, H.; et al. Suppression of temperature quenching in perovskite nanocrystals for efficient and thermally stable light-emitting diodes. *Nat. Photonics* **2021**, *15*, 379–385.
32. Wang, H.; Kim, D.H. Perovskite-based photodetectors: Materials and devices. *Chem. Soc. Rev.* **2017**, *46*, 5204–5236.
33. Gong, M.; Sakidja, R.; Goul, R.; et al. High-Performance All-Inorganic $CsPbCl_3$ Perovskite Nanocrystal Photodetectors with Superior Stability. *ACS Nano* **2019**, *13*, 1772–1783.
34. Chen, Q.; Wu, J.; Ou, X.; et al. All-inorganic perovskite nanocrystal scintillators. *Nature* **2018**, *561*, 88–93.
35. Zhu, C.; Boehme, S.; Feld, L.; et al. Single-photon superradiance in individual caesium lead halide quantum dots. *Nature* **2024**, *626*, 535–541.
36. Zhou, Q.; Bai, Z.; Lu, W.; et al. In Situ Fabrication of Halide Perovskite Nanocrystal-Embedded Polymer Composite Films with Enhanced Photoluminescence for Display Backlights. *Adv. Mater.* **2016**, *28*, 9163–9168.
37. Kim, Y.C.; Kim, K.H.; Son, D.-Y.; et al. Printable organometallic perovskite enables large-area, low-dose X-ray imaging. *Nature* **2017**, *550*, 87–91.
38. Li, X.; Wu, Y.; Zhang, S.; et al. $CsPbX_3$ Quantum Dots for Lighting and Displays: Room-Temperature Synthesis, Photoluminescence Superiorities, Underlying Origins and White Light-Emitting Diodes. *Adv. Funct. Mater.* **2016**, *26*, 2435–2445.
39. Xue, J.; Wang, R.; Yang, Y. The surface of halide perovskites from nano to bulk. *Nat. Rev. Mater.* **2020**, *5*, 809–827.
40. Akkerman, Q.A.; Rainò, G.; Kovalenko, M.V.; et al. Genesis, challenges and opportunities for colloidal lead halide perovskite nanocrystals. *Nat. Mater.* **2018**, *17*, 394–405.
41. Swarnkar, A.; Chulliyil, R.; Ravi, V.; et al. Colloidal $CsPbBr_3$ Perovskite Nanocrystals: Luminescence beyond Traditional Quantum Dots. *Angew. Chem., Int. Ed.* **2015**, *54*, 15424–15428.

42. Malgras, V.; Tominaka, S.; Ryan, J.; et al. Observation of Quantum Confinement in Monodisperse Methylammonium Lead Halide Perovskite Nanocrystals Embedded in Mesoporous Silica. *J. Am. Chem. Soc.* **2016**, *138*, 13874–13881.
43. Butkus, J.; Vashishtha, P.; Chen, K.; et al. The Evolution of Quantum Confinement in $CsPbBr_3$ Perovskite Nanocrystals. *Chem. Mater.* **2017**, *29*, 3644–3652.
44. Dong, Y.; Qiao, T.; Kim, D.; et al. Precise Control of Quantum Confinement in Cesium Lead Halide Perovskite Quantum Dots via Thermodynamic Equilibrium. *Nano Lett.* **2018**, *18*, 3716–3722.
45. Vighnesh, K.; Wang, S.; Liu, H.; et al. Hot-Injection Synthesis Protocol for Green-Emitting Cesium Lead Bromide Perovskite Nanocrystals. *ACS Nano* **2022**, *16*, 19618–19625.
46. Protesescu, L.; Yakunin, S.; Bodnarchuk, M.I.; et al. Nanocrystals of Cesium Lead Halide Perovskites ($CsPbX_3$, X = Cl, Br, and I): Novel Optoelectronic Materials Showing Bright Emission with Wide Color Gamut. *Nano Lett.* **2015**, *15*, 3692–3696.
47. Sun, S.; Yuan, D.; Xu, Y.; et al. Ligand-Mediated Synthesis of Shape-Controlled Cesium Lead Halide Perovskite Nanocrystals via Reprecipitation Process at Room Temperature. *ACS Nano* **2016**, *10*, 3648–3657.
48. Zhang, F.; Zhong, H.; Chen, C.; et al. Brightly Luminescent and Color-Tunable Colloidal $CH_3NH_3PbX_3$ (X = Br, I, Cl) Quantum Dots: Potential Alternatives for Display Technology. *ACS Nano* **2015**, *9*, 4533–4542.
49. Huang, H.; Bodnarchuk, M.I.; Kershaw, S.V.; et al. Lead Halide Perovskite Nanocrystals in the Research Spotlight: Stability and Defect Tolerance. *ACS Energy Lett.* **2017**, *2*, 2071–2083.
50. Walsh, A.; Zunger, A. Instilling defect tolerance in new compounds. *Nat. Mater.* **2017**, *16*, 964–967.
51. Liu, F.; Zhang, Y.; Ding, C.; et al. Highly Luminescent Phase-Stable $CsPbI_3$ Perovskite Quantum Dots Achieving Near 100% Absolute Photoluminescence Quantum Yield. *ACS Nano* **2017**, *11*, 10373–10383.
52. Tong, Y.; Bladt, E.; Aygüler, M.F.; et al. Highly Luminescent Cesium Lead Halide Perovskite Nanocrystals with Tunable Composition and Thickness by Ultrasonication. *Angew. Chem., Int. Ed.* **2016**, *55*, 13887–13892.
53. Gonzalez-Carrero, S.; Francés-Soriano, L.; González-Béjar, M.; et al. The Luminescence of $CH_3NH_3PbBr_3$ Perovskite Nanoparticles Crests the Summit and Their Photostability under Wet Conditions is Enhanced. *Small* **2016**, *12*, 5245–5250.
54. Jin, C.H.; Regan, E.C.; Yan, A.M.; et al. Observation of moire excitons in WSe_2/WS_2 heterostructure superlattices. *Nature* **2019**, *567*, 76–80.
55. Li, T.X.; Jiang, S.W.; Li, L.Z.; et al. Continuous Mott transition in semiconductor moire superlattices. *Nature* **2021**, *597*, 350–354.
56. Liu, E.R.; Barré, E.; van Baren, J.; et al. Signatures of moire trions in $WSe_2/MoSe_2$ heterobilayers. *Nature* **2021**, *594*, 46–50.
57. Wan, S.Y.; Xia, X.Y.; Gao, Y.T.; et al. Curvature-guided depletion stabilizes Kagome superlattices of nanocrystals. *Science* **2025**, *387*, 978–984.
58. Becker, M.A.; Vaxenburg, R.; Nedelcu, G.; et al. Bright triplet excitons in caesium lead halide perovskites. *Nature* **2018**, *553*, 189–193.
59. Becker, M.A.; Scarpelli, L.; Nedelcu, G.; et al. Long Exciton Dephasing Time and Coherent Phonon Coupling in $CsPbBr_2Cl$ Perovskite Nanocrystals. *Nano Lett.* **2018**, *18*, 7546–7551.
60. Cherniukh, I.; Rainò, G.; Stöferle, T.; et al. Perovskite-type superlattices from lead halide perovskite nanocubes. *Nature* **2021**, *593*, 535–542.
61. Dey, A.; Ye, J.; De, A.; et al. State of the Art and Prospects for Halide Perovskite Nanocrystals. *ACS Nano* **2021**, *15*, 10775–10981.
62. Otero-Martínez, C.; Ye, J.; Sung, J.; et al. Colloidal Metal-Halide Perovskite Nanoplatelets: Thickness-Controlled Synthesis, Properties, and Application in Light-Emitting Diodes. *Adv. Mater.* **2022**, *34*, 2107105.
63. Yang, D.; Li, X.; Zeng, H. Surface Chemistry of All Inorganic Halide Perovskite Nanocrystals: Passivation Mechanism and Stability. *Adv. Mater. Interfaces* **2018**, *5*, 1701662.
64. Shamsi, J.; Urban, A.S.; Imran, M.; et al. Metal Halide Perovskite Nanocrystals: Synthesis, Post-Synthesis Modifications, and Their Optical Properties. *Chem. Rev.* **2019**, *119*, 3296–3348.
65. Chouhan, L.; Ghimire, S.; Subrahmanyam, C.; et al. Synthesis, optoelectronic properties and applications of halide perovskites. *Chem. Soc. Rev.* **2020**, *49*, 2869–2885.
66. Zhang, Y.; Siegler, T.; Thomas, C.; et al. A "Tips and Tricks" Practical Guide to the Synthesis of Metal Halide Perovskite Nanocrystals. *Chem. Mater.* **2020**, *32*, 5410–5423.
67. Kovalenko, M.V.; Protesescu, L.; Bodnarchuk, M.I. Properties and potential optoelectronic applications of lead halide perovskite nanocrystals. *Science* **2017**, *358*, 745–750.
68. Liu, Z.; Qin, X.; Chen, Q.H.; et al. Metal-Halide Perovskite Nanocrystal Superlattice: Self-Assembly and Optical Fingerprints. *Adv. Mater.* **2023**, *35*, 2209279.
69. Yan, D.N.; Shan, Q.S.; Dong, Y.H.; et al. Perovskite nanocrystal superlattices: Self-assembly, collective behavior, and applications. *Chem. Commun.* **2023**, *59*, 5365–5374.

70. Yang, Z.; Peng, S.; Lin, F.; et al. Self-assembly Behavior of Metal Halide Perovskite Nanocrystals. *Chin. J. Chem.* **2022**, *40*, 2239–2248.
71. Li, Y.; Zhang, F. Self-assembly of perovskite nanocrystals: From driving forces to applications. *J. Energy Chem.* **2024**, *88*, 561–578.
72. Sun, S.; Lu, M.; Lu, P.; et al. Perovskite nanocrystal superlattices and their application in light-emitting devices. *Mater. Sci. Eng. : R: Rep.* **2025**, *164*, 100984.
73. De Roo, J.; Ibáñez, M.; Geiregat, P.; et al. Highly Dynamic Ligand Binding and Light Absorption Coefficient of Cesium Lead Bromide Perovskite Nanocrystals. *ACS Nano* **2016**, *10*, 2071–2081.
74. Xue, J.; Lee, J.-W.; Dai, Z.; et al. Surface Ligand Management for Stable $FAPbI_3$ Perovskite Quantum Dot Solar Cells. *Joule* **2018**, *2*, 1866–1878.
75. Imran, M.; Ijaz, P.; Baranov, D.; et al. Shape-Pure, Nearly Monodispersed $CsPbBr_3$ Nanocubes Prepared Using Secondary Aliphatic Amines. *Nano Lett.* **2018**, *18*, 7822–7831.
76. Dutta, A.; Dutta, S.; Das Adhikari, S.; et al. Tuning the Size of $CsPbBr_3$ Nanocrystals: All at One Constant Temperature. *ACS Energy Lett.* **2018**, *3*, 329–334.
77. Bekenstein, Y.; Koscher, B.A.; Eaton, S.W.; et al. Highly Luminescent Colloidal Nanoplates of Perovskite Cesium Lead Halide and Their Oriented Assemblies. *J. Am. Chem. Soc.* **2015**, *137*, 16008–16011.
78. Akkerman, Q.A.; Nguyen, T.P.T.; Boehme, S.C.; et al. Controlling the nucleation and growth kinetics of lead halide perovskite quantum dots. *Science* **2022**, *377*, 1406–1412.
79. Zhang, D.; Eaton, S.W.; Yu, Y.; et al. Solution-Phase Synthesis of Cesium Lead Halide Perovskite Nanowires. *J. Am. Chem. Soc.* **2015**, *137*, 9230–9233.
80. Pan, A.Z.; He, B.; Fan, X.Y.; et al. Insight into the Ligand-Mediated Synthesis of Colloidal $CsPbBr_3$ Perovskite Nanocrystals: The Role of Organic Acid, Base, and Cesium Precursors. *ACS Nano* **2016**, *10*, 7943–7954.
81. Almeida, G.; Goldoni, L.; Akkerman, Q.; et al. Role of Acid–Base Equilibria in the Size, Shape, and Phase Control of Cesium Lead Bromide Nanocrystals. *ACS Nano* **2018**, *12*, 1704–1711.
82. Zhang, X.; Bai, X.; Wu, H.; et al. Water-Assisted Size and Shape Control of $CsPbBr_3$ Perovskite Nanocrystals. *Angew. Chem., Int. Ed.* **2018**, *57*, 3337–3342.
83. Bertolotti, F.; Nedelcu, G.; Vivani, A.; et al. Crystal Structure, Morphology, and Surface Termination of Cyan-Emissive, Six-Monolayers-Thick $CsPbBr_3$ Nanoplatelets from X-ray Total Scattering. *ACS Nano* **2019**, *13*, 14294–14307.
84. Bera, S.; Behera, R.K.; Pradhan, N. α-Halo Ketone for Polyhedral Perovskite Nanocrystals: Evolutions, Shape Conversions, Ligand Chemistry, and Self-Assembly. *J. Am. Chem. Soc.* **2020**, *142*, 20865–20874.
85. Zhu, F.; Men, L.; Guo, Y.J.; et al. Shape Evolution and Single Particle Luminescence of Organometal Halide Perovskite Nanocrystals. *ACS Nano* **2015**, *9*, 2948–2959.
86. Imran, M.; Caligiuri, V.; Wang, M.; et al. Benzoyl Halides as Alternative Precursors for the Colloidal Synthesis of Lead-Based Halide Perovskite Nanocrystals. *J. Am. Chem. Soc.* **2018**, *140*, 2656–2664.
87. Tang, X.; Zu, Z.; Shao, H.; et al. All-inorganic perovskite $CsPb(Br/I)_3$ nanorods for optoelectronic application. *Nanoscale* **2016**, *8*, 15158–15161.
88. Chen, Y.; Zhao, L.; Peng, L.; et al. Solution-phase synthesis of $CsPbI_3$ nanowire clusters via polymer-induced anisotropic growth and self-assembly. *Chem. Commun.* **2019**, *55*, 8266–8269.
89. Song, J.; Xu, L.; Li, J.; et al. Monolayer and Few-Layer All-Inorganic Perovskites as a New Family of Two-Dimensional Semiconductors for Printable Optoelectronic Devices. *Adv. Mater.* **2016**, *28*, 4861–4869.
90. Bohn, B.J.; Tong, Y.; Gramlich, M.; et al. Boosting Tunable Blue Luminescence of Halide Perovskite Nanoplatelets through Postsynthetic Surface Trap Repair. *Nano Lett.* **2018**, *18*, 5231–5238.
91. Akkerman, Q.A.; Motti, S.G.; Kandada, A.R.S.; et al. Solution Synthesis Approach to Colloidal Cesium Lead Halide Perovskite Nanoplatelets with Monolayer-Level Thickness Control. *J. Am. Chem. Soc.* **2016**, *138*, 1010–1016.
92. Bai, Y.; Hao, M.; Ding, S.; et al. Surface Chemistry Engineering of Perovskite Quantum Dots: Strategies, Applications, and Perspectives. *Adv. Mater.* **2022**, *34*, 2105958.
93. Grisorio, R.; Di Clemente, M.; Fanizza, E.; et al. Exploring the surface chemistry of cesium lead halide perovskite nanocrystals. *Nanoscale* **2019**, *11*, 986–999.
94. DuBose, J.; Kamat, P. Directing Energy Transfer in Halide Perovskite-Chromophore Hybrid Assemblies. *J. Am. Chem. Soc.* **2021**, *143*, 19214–19223.
95. Boles, M.A.; Engel, M.; Talapin, D.V. Self-Assembly of Colloidal Nanocrystals: From Intricate Structures to Functional Materials. *Chem. Rev.* **2016**, *116*, 11220–11289.
96. Nenon, D.; Pressler, K.; Kang, J.; et al. Design Principles for Trap-Free $CsPbX_3$ Nanocrystals: Enumerating and Eliminating Surface Halide Vacancies with Softer Lewis Bases. *J. Am. Chem. Soc.* **2018**, *140*, 17760–17772.
97. Krieg, F.; Ochsenbein, S.T.; Yakunin, S.; et al. Colloidal $CsPbX_3$ (X = Cl, Br, I) Nanocrystals 2.0: Zwitterionic Capping Ligands for Improved Durability and Stability. *ACS Energy Lett.* **2018**, *3*, 641–646.

98. Mir, W.J.; Alamoudi, A.; Yin, J.; et al. Lecithin Capping Ligands Enable Ultrastable Perovskite-Phase $CsPbI_3$ Quantum Dots for Rec. 2020 Bright-Red Light-Emitting Diodes. *J. Am. Chem. Soc.* **2022**, *144*, 13302–13310.
99. Grisorio, R.; Fasulo, F.; Muñoz-García, A.B.; et al. In Situ Formation of Zwitterionic Ligands: Changing the Passivation Paradigms of $CsPbBr_3$ Nanocrystals. *Nano Lett.* **2022**, *22*, 4437–4444.
100. Morad, V.; Stelmakh, A.; Svyrydenko, M.; et al. Designer phospholipid capping ligands for soft metal halide nanocrystals. *Nature* **2023**, *626*, 542–548.
101. Haydous, F.; Gardner, J.; Cappel, U. The impact of ligands on the synthesis and application of metal halide perovskite nanocrystals. *J. Mater. Chem. A* **2021**, *9*, 23419–23443.
102. Bodnarchuk, M.; Boehme, S.; ten Brinck, S.; et al. Rationalizing and Controlling the Surface Structure and Electronic Passivation of Cesium Lead Halide Nanocrystals. *ACS Energy Lett.* **2019**, *4*, 63–74.
103. ten Brinck, S.; Infante, I. Surface Termination, Morphology, and Bright Photoluminescence of Cesium Lead Halide Perovskite Nanocrystals. *ACS Energy Lett.* **2016**, *1*, 1266–1272.
104. Cheng, W.L.; Campolongo, M.J.; Cha, J.J.; et al. Free-standing nanoparticle superlattice sheets controlled by DNA. *Nat. Mater.* **2009**, *8*, 519–525.
105. Jones, M.R.; Macfarlane, R.J.; Lee, B.; et al. DNA-nanoparticle superlattices formed from anisotropic building blocks. *Nat. Mater.* **2010**, *9*, 913–917.
106. Shi, J.; Li, F.; Jin, Y.; et al. In Situ Ligand Bonding Management of $CsPbI_3$ Perovskite Quantum Dots Enables High-Performance Photovoltaics and Red Light-Emitting Diodes. *Angew. Chem., Int. Ed.* **2020**, *59*, 22230–22237.
107. Park, J.; Lee, A.; Yu, J.; et al. Surface Ligand Engineering for Efficient Perovskite Nanocrystal-Based Light-Emitting Diodes. *ACS Appl. Mater. Interfaces* **2019**, *11*, 8428–8435.
108. Tan, Y.; Zou, Y.; Wu, L.; et al. Highly Luminescent and Stable Perovskite Nanocrystals with Octylphosphonic Acid as a Ligand for Efficient Light-Emitting Diodes. *ACS Appl. Mater. Interfaces* **2018**, *10*, 3784–3792.
109. Imran, M.; Ijaz, P.; Goldoni, L.; et al. Simultaneous Cationic and Anionic Ligand Exchange For Colloidally Stable $CsPbBr_3$ Nanocrystals. *ACS Energy Lett.* **2019**, *4*, 819–824.
110. Shynkarenko, Y.; Bodnarchuk, M.I.; Bernasconi, C.; et al. Direct Synthesis of Quaternary Alkylammonium-Capped Perovskite Nanocrystals for Efficient Blue and Green Light-Emitting Diodes. *ACS Energy Lett.* **2019**, *4*, 2703–2711.
111. Li, X.; Cai, W.; Guan, H.; et al. Highly stable $CsPbBr_3$ quantum dots by silica-coating and ligand modification for white light-emitting diodes and visible light communication. *Chem. Eng. J.* **2021**, *419*, 129551.
112. Huang, Y.; Luan, W.; Liu, M.; et al. DDAB-assisted synthesis of iodine-rich $CsPbI_3$ perovskite nanocrystals with improved stability in multiple environments. *J. Mater. Chem. C* **2020**, *8*, 2381–2387.
113. Fiuza-Maneiro, N.; Sun, K.; López-Fernández, I.; et al. Ligand Chemistry of Inorganic Lead Halide Perovskite Nanocrystals. *ACS Energy Lett.* **2023**, *8*, 1152–1191.
114. Zhao, H.; Chen, H.; Bai, S.; et al. High-Brightness Perovskite Light-Emitting Diodes Based on $FAPbBr_3$ Nanocrystals with Rationally Designed Aromatic Ligands. *ACS Energy Lett.* **2021**, *6*, 2395–2403.
115. De, A.; Mondal, N.; Samanta, A. Hole Transfer Dynamics from Photoexcited Cesium Lead Halide Perovskite Nanocrystals: 1-Aminopyrene as Hole Acceptor. *J. Phys. Chem. C* **2018**, *122*, 13617–13623.
116. Lee, H.; Yoon, D.E.; Koh, S.; et al. Ligands as a universal molecular toolkit in synthesis and assembly of semiconductor nanocrystals. *Chem. Sci.* **2020**, *11*, 2318–2329.
117. Koscher, B.A.; Swabeck, J.K.; Bronstein, N.D.; et al. Essentially Trap-Free $CsPbBr_3$ Colloidal Nanocrystals by Postsynthetic Thiocyanate Surface Treatment. *J. Am. Chem. Soc.* **2017**, *139*, 6566–6569.
118. Rainò, G.; Becker, M.A.; Bodnarchuk, M.I.; et al. Superfluorescence from lead halide perovskite quantum dot superlattices. *Nature* **2018**, *563*, 671–675.
119. Zhang, D.D.; Yu, Y.; Bekenstein, Y.; et al. Ultrathin Colloidal Cesium Lead Halide Perovskite Nanowires. *J. Am. Chem. Soc.* **2016**, *138*, 13155–13158.
120. Yang, X.; Li, F.; Wang, X.; et al. In situ tetrafluoroborate-modified $MAPbBr_3$ nanocrystals showing high photoluminescence, stability and self-assembly behavior. *J. Mater. Chem. C* **2020**, *8*, 1989–1997.
121. Moral, R.F.; Malfatti-Gasperini, A.A.; Bonato, L.G.; et al. Self-assembly of perovskite nanoplates in colloidal suspensions. *Mater. Horiz.* **2023**, *10*, 5822–5834.
122. Kobiyama, E.; Urbonas, D.; Aymoz, B.; et al. Perovskite Nanocrystal Self-Assemblies in 3D Hollow Templates. *ACS Nano* **2025**, *19*, 6748–6757.
123. Li, D.S.; Chen, Q.; Chun, J.; et al. Nanoparticle Assembly and Oriented Attachment: Correlating Controlling Factors to the Resulting Structures. *Chem. Rev.* **2023**, *123*, 3127–3159.
124. Murray, C.B.; Kagan, C.R.; Bawendi, M.G. Self-organization of CdSe Nanocrystallites into Three-Dimensional Quantum Dot Superlattices. *Science* **1995**, *270*, 1335–1338.
125. Bodnarchuk, M.I.; Kovalenko, M.V.; Heiss, W.; et al. Energetic and Entropic Contributions to Self-Assembly of Binary Nanocrystal Superlattices: Temperature as the Structure-Directing Factor. *J. Am. Chem. Soc.* **2010**, *132*, 11967–11977.

126. Ji, Y.; Wang, M.; Yang, Z.; et al. Nanowire-assisted self-assembly of one-dimensional nanocrystal superlattice chains. *J. Mater. Chem. C* **2019**, *7*, 8471–8476.
127. Levy, S.; Be'er, O.; Shaek, S.; et al. Collective Interactions of Quantum-Confined Excitons in Halide Perovskite Nanocrystal Superlattices. *ACS Nano* **2024**, *19*, 963–971.
128. Zhang, X.; Lv, L.; Ji, L.; et al. Self-Assembly of One-Dimensional Nanocrystal Superlattice Chains Mediated by Molecular Clusters. *J. Am. Chem. Soc.* **2016**, *138*, 3290–3293.
129. Wang, K.-H.; Yang, J.-N.; Ni, Q.-K.; et al. Metal Halide Perovskite Supercrystals: Gold–Bromide Complex Triggered Assembly of $CsPbBr_3$ Nanocubes. *Langmuir* **2018**, *34*, 595–602.
130. Jones, M.R.; Seeman, N.C.; Mirkin, C.A. Programmable materials and the nature of the DNA bond. *Science* **2015**, *347*, 6224.
131. Lin, Q.Y.; Mason, J.A.; Li, Z.Y.; et al. Building superlattices from individual nanoparticles via template-confined DNA-mediated assembly. *Science* **2018**, *359*, 669–672.
132. Zhou, W.J.; Li, Y.W.; Je, K.; et al. Space-tiled colloidal crystals from DNA-forced shape-complementary polyhedra pairing. *Science* **2024**, *383*, 312–319.
133. Jana, A.; Kim, K. Effect of Organic-Cation Exchange Reaction of Perovskites in Water: H-Bond Assisted Self-Assembly, Black Phase Stabilization, and Single-Particle Imaging. *ACS Appl. Energy Mater.* **2019**, *2*, 4496–4503.
134. Anderson, V.J.; Lekkerkerker, H.N.W. Insights into phase transition kinetics from colloid science. *Nature* **2002**, *416*, 811–815.
135. Clark, D.E.; Lumsargis, V.A.; Blach, D.D.; et al. Quantifying Structural Heterogeneity in Individual $CsPbBr_3$ Quantum Dot Superlattices. *Chem. Mater.* **2022**, *34*, 10200–10207.
136. Travesset, A. Topological structure prediction in binary nanoparticle superlattices. *Soft Matter* **2017**, *13*, 147–157.
137. Coropceanu, I.; Boles, M.A.; Talapin, D.V. Systematic Mapping of Binary Nanocrystal Superlattices: The Role of Topology in Phase Selection. *J. Am. Chem. Soc.* **2019**, *141*, 5728–5740.
138. Hallstrom, J.; Cherniukh, I.; Zha, X.; et al. Ligand Effects in Assembly of Cubic and Spherical Nanocrystals: Applications to Packing of Perovskite Nanocubes. *ACS Nano* **2023**, *17*, 7219–7228.
139. Boles, M.A.; Talapin, D.V. Many-Body Effects in Nanocrystal Superlattices: Departure from Sphere Packing Explains Stability of Binary Phases. *J. Am. Chem. Soc.* **2015**, *137*, 4494–4502.
140. Travesset, A. Soft Skyrmions, Spontaneous Valence and Selection Rules in Nanoparticle Superlattices. *ACS Nano* **2017**, *11*, 5375–5382.
141. Lapointe, V.; Green, P.B.; Chen, A.N.; et al. Long live(d) $CsPbBr_3$ superlattices: Colloidal atomic layer deposition for structural stability. *Chem. Sci.* **2024**, *15*, 4510–4518.
142. Boehme, S.C.; Bodnarchuk, M.I.; Burian, M.; et al. Strongly Confined $CsPbBr_3$ Quantum Dots as Quantum Emitters and Building Blocks for Rhombic Superlattices. *ACS Nano* **2023**, *17*, 2089–2100.
143. Zhang, M.Q.; Hu, J.C.; Xi, G.Q.; et al. Colloidal Perovskite Nanocrystal Superlattice Films with Simultaneous Polarized Emission and Orderly Electric Polarity via an In Situ Surface Cross-Linking Reaction. *ACS Nano* **2025**, *19*, 7283–7293.
144. Yin, T.T.; Yan, H.J.; Abdelwahab, I.; et al. Pressure driven rotational isomerism in 2D hybrid perovskites. *Nat. Commun.* **2023**, *14*, 411.
145. Li, Z.W.; Fan, Q.S.; Yin, Y.D. Colloidal Self-Assembly Approaches to Smart Nanostructured Materials. *Chem. Rev.* **2022**, *122*, 4976–5067.
146. Tong, Y.; Yao, E.P.; Manzi, A.; et al. Spontaneous Self-Assembly of Perovskite Nanocrystals into Electronically Coupled Supercrystals: Toward Filling the Green Gap. *Adv. Mater.* **2018**, *30*, 1801117.
147. Hazra, V.; Mondal, S.; Pattanayak, P.; et al. Nanoplatelet Superlattices by Tin-Induced Transformation of $FAPbI_3$ Nanocrystals. *Small* **2024**, *20*, 2304920.
148. Ferreira, M.G.; Gastin, B.; Hiller, J.; et al. Self-Assembly of Quantum-Confined $CsPbBr_3$ Perovskite Nanocrystals into Rhombic, Frame, and Rectangular Superlattices. *Small Struct.* **2025**, *6*, 2500133.
149. Pan, A.Z.; Jurow, M.; Zhao, Y.R.; et al. Templated self-assembly of one-dimensional $CsPbX_3$ perovskite nanocrystal superlattices. *Nanoscale* **2017**, *9*, 17688–17693.
150. Liu, Y.; Siron, M.; Lu, D.L.; et al. Self-Assembly of Two-Dimensional Perovskite Nanosheet Building Blocks into Ordered Ruddlesden-Popper Perovskite Phase. *J. Am. Chem. Soc.* **2019**, *141*, 13028–13032.
151. Mehetor, S.K.; Ghosh, H.; Pradhan, N. Acid–Amine Equilibria for Formation and Long-Range Self-Organization of Ultrathin $CsPbBr_3$ Perovskite Platelets. *J. Phys. Chem. Lett.* **2019**, *10*, 1300–1305.
152. Ye, J.; Ren, A.; Dai, L.; et al. Direct linearly polarized electroluminescence from perovskite nanoplatelet superlattices. *Nat. Photonics* **2024**, *18*, 586–594.
153. Tisdale, W.A. Twisted perovskite layers come together. *Nat. Mater.* **2024**, *23*, 1155–1156.
154. Zhang, S.; Jin, L.; Lu, Y.; et al. Moiré superlattices in twisted two-dimensional halide perovskites. *Nat. Mater.* **2024**, *23*, 1222–1229.

155. Jin, F.; Ren, J.H.; Zanotti, S.; et al. Exciton polariton condensation in a perovskite moiré flat band at room temperature. *Sci. Adv.* **2025**, 11, eadx2361.
156. Zhan, G.; Koek, B.; Yuan, Y.; et al. Moiré two-dimensional covalent organic framework superlattices. *Nat. Chem.* **2025**, *17*, 518–524.
157. Chen, D.X.; Lian, Z.; Huang, X.; et al. Excitonic insulator in a heterojunction moire superlattice. *Nat. Phys.* **2022**, *18*, 1171–1176.
158. Huang, X.; Wang, T.M.; Miao, S.N.; et al. Correlated insulating states at fractional fillings of the WS_2/WSe_2 moire lattice. *Nat. Phys.* **2021**, *17*, 715–719.
159. Li, H.Y.; Li, S.W.; Naik, M.H.; et al. Imaging local discharge cascades for correlated electrons in WS_2/WSe_2 moire superlattices. *Nat. Phys.* **2021**, *17*, 1114–1119.
160. Cao, Y.; Rodan-Legrain, D.; Rubies-Bigorda, O.; et al. Tunable correlated states and spin-polarized phases in twisted bilayer-bilayer graphene. *Nature* **2020**, *583*, 215–220.
161. Sekh, T.V.; Cherniukh, I.; Kobiyama, E.; et al. All-Perovskite Multicomponent Nanocrystal Superlattices. *ACS Nano* **2024**, *18*, 8423–8436.
162. Cherniukh, I.; Rainò, G.; Sekh, T.V.; et al. Shape-Directed Co-Assembly of Lead Halide Perovskite Nanocubes with Dielectric Nanodisks into Binary Nanocrystal Superlattices. *ACS Nano* **2021**, *15*, 16488–16500.
163. Cherniukh, I.; Sekh, T.V.; Rainò, G.; et al. Structural Diversity in Multicomponent Nanocrystal Superlattices Comprising Lead Halide Perovskite Nanocubes. *ACS Nano* **2022**, *16*, 7210–7232.
164. Yang, S.; Yang, D.-B.; Ning, Y.; et al. Super-expansive thermo-reversible interstitial solid solution of nanocrystal superlattices with mesogens. *Nat. Mater.* **2026**, *25*, 294–301.
165. Jiang, Y.X.; Niu, J.G.; Wang, C.; et al. Experimental demonstration of tunable hybrid improper ferroelectricity in double-perovskite superlattice films. *Nat. Commun.* **2024**, *15*, 5549.
166. Lapkin, D.; Kirsch, C.; Hiller, J.; et al. Spatially resolved fluorescence of caesium lead halide perovskite supercrystals reveals quasi-atomic behavior of nanocrystals. *Nat. Commun.* **2022**, *13*, 892.
167. Gao, Y.; Shi, E.Z.; Deng, S.B.; et al. Molecular engineering of organic-inorganic hybrid perovskites quantum wells. *Nat. Chem.* **2019**, *11*, 1151–1157.
168. Zhou, C.; Zhong, Y.; Dong, H.; et al. Cooperative excitonic quantum ensemble in perovskite-assembly superlattice microcavities. *Nat. Commun.* **2020**, *11*, 329.
169. Hong, K.S.; Chen, O.; Bai, Y.S. Emergent quantum properties from low-dimensional building blocks and their superlattices. *Nano Res.* **2024**, *17*, 10490–10510.
170. Wang, Q.; Tan, J.; Jie, Q.; et al. Perturbation-driven echo-like superfluorescence in perovskite superlattices. *Adv. Photonics* **2023**, *5*, 055001.
171. Krieg, F.; Sercel, P.C.; Burian, M.; et al. Monodisperse Long-Chain Sulfobetaine-Capped $CsPbBr_3$ Nanocrystals and Their Superfluorescent Assemblies. *ACS Cent. Sci.* **2021**, *7*, 135–144.
172. Russ, B.; Eisler, C.N. The future of quantum technologies: Superfluorescence from solution-processed, tunable materials. *Nanophotonics* **2024**, *13*, 1943–1951.
173. Lei, Y.S.; Li, Y.H.; Lu, C.C.F.; et al. Perovskite superlattices with efficient carrier dynamics. *Nature* **2022**, *608*, 317–323.
174. Blach, D.D.; Lumsargis-Roth, V.A.; Chuang, C.; et al. Environment-assisted quantum transport of excitons in perovskite nanocrystal superlattices. *Nat. Commun.* **2025**, *16*, 1270.
175. Baranov, D.; Fieramosca, A.; Yang, R.X.; et al. Aging of Self-Assembled Lead Halide Perovskite Nanocrystal Superlattices: Effects on Photoluminescence and Energy Transfer. *ACS Nano* **2020**, *15*, 650–664.
176. Erdem, O.; Gungor, K.; Guzelturk, B.; et al. Orientation-Controlled Nonradiative Energy Transfer to Colloidal Nanoplatelets: Engineering Dipole Orientation Factor. *Nano Lett.* **2019**, *19*, 4297–4305.
177. Penzo, E.; Loiudice, A.; Barnard, E.S.; et al. Long-Range Exciton Diffusion in Two-Dimensional Assemblies of Cesium Lead Bromide Perovskite Nanocrystals. *ACS Nano* **2020**, *14*, 6999–7007.
178. Kumar, S.; Marcato, T.; Krumeich, F.; et al. Anisotropic nanocrystal superlattices overcoming intrinsic light outcoupling efficiency limit in perovskite quantum dot light-emitting diodes. *Nat. Commun.* **2022**, *13*, 2106.
179. Kovalenko, M.V.; Bodnarchuk, M.I. Lead Halide Perovskite Nanocrystals: From Discovery to Self-assembly and Applications. *Chimia* **2017**, *71*, 461–470.
180. Jagielski, J.; Solari, S.F.; Jordan, L.; et al. Scalable photonic sources using two-dimensional lead halide perovskite superlattices. *Nat. Commun.* **2020**, *11*, 387.
181. Udayabhaskararao, T.; Altantzis, T.; Houben, L.; et al. Tunable porous nanoallotropes prepared by post-assembly etching of binary nanoparticle superlattices. *Science* **2017**, *358*, 514–518.
182. Tang, Z.Y.; Zhang, Z.L.; Wang, Y.; et al. Self-assembly of CdTe nanocrystals into free-floating sheets. *Science* **2006**, *314*, 274–278.

183. Song, T.C.; Sun, Q.C.; Anderson, E.; et al. Direct visualization of magnetic domains and moire magnetism in twisted 2D magnets. *Science* **2021**, *374*, 1140–1144.
184. Xie, H.C.; Luo, X.P.; Ye, Z.P.; et al. Evidence of non-collinear spin texture in magnetic moire superlattices. *Nat. Phys.* **2023**, *19*, 1150–1155.
185. Deng, S.B.; Park, H.; Reimann, J.; et al. Frozen non-equilibrium dynamics of exciton Mott insulators in moiré superlattices. *Nat. Mater.* **2025**, *24*, 527–534.
186. Du, L.J.; Huang, Z.H.; Zhang, J.; et al. Nonlinear physics of moiré superlattices. *Nat. Mater.* **2024**, *23*, 1179–1192.
187. Fortin-Deschênes, M.; Watanabe, K.; Taniguchi, T.; et al. Van der Waals epitaxy of tunable moires enabled by alloying. *Nat. Mater.* **2024**, *23*, 339–346.
188. Ribeiro-Palau, R.; Zhang, C.J.; Watanabe, K.; et al. Twistable electronics with dynamically rotatable heterostructures. *Science* **2018**, *361*, 690–693.
189. Quan, J.M.; Linhart, L.; Lin, M.L.; et al. Phonon renormalization in reconstructed MoS_2 moire superlattices. *Nat. Mater.* **2021**, *20*, 1100–1105.
190. Ni, G.X.; Wang, H.; Wu, J.S.; et al. Plasmons in graphene moire superlattices. *Nat. Mater.* **2015**, *14*, 1217–1222.
191. Chen, M.Y.; Lin, X.; Dinh, T.H.; et al. Configurable phonon polaritons in twisted α-MoO_3. *Nat. Mater.* **2020**, *19*, 1307–1311.
192. Foutty, B.A.; Yu, J.C.; Devakul, T.; et al. Tunable spin and valley excitations of correlated insulators in Γ-valley moire bands. *Nat. Mater.* **2023**, *22*, 731–736.
193. Qian, C.; Stanifer, E.; Ma, Z.; et al. Nanoscale phonon dynamics in self-assembled nanoparticle lattices. *Nat. Mater.* **2025**, *24*, 1616–1625.
194. Huang, D.; Choi, J.; Shih, C.K.; et al. Excitons in semiconductor moire superlattices. *Nat. Nanotechnol.* **2022**, *17*, 227–238.
195. Li, Z.W.; Lim, Y.; Tanriover, I.; et al. DNA-mediated assembly of Au bipyramids into anisotropic light emitting kagome superlattices. *Sci. Adv.* **2024**, 10, eadp3756.
196. Ross, M.B.; Ku, J.C.; Vaccarezza, V.M.; et al. Nanoscale form dictates mesoscale function in plasmonic DNA-nanoparticle superlattices. *Nat. Nanotechnol.* **2015**, *10*, 453–458.
197. Rogers, W.B.; Shih, W.M.; Manoharan, V.N. Using DNA to program the self-assembly of colloidal nanoparticles and microparticles. *Nat. Rev. Mater.* **2016**, *1*, 16008.
198. Kim, A.; Kim, C.; Waltmann, T.; et al. Patchy nanoparticles by atomic stencilling. *Nature* **2025**, *646*, 592–600.
199. Zhao, B.; Wan, Z.; Liu, Y.; et al. High-order superlattices by rolling up van der Waals heterostructures. *Nature* **2021**, *591*, 385–390.
200. Wang, Q.; Wang, Z.P.; Li, Z.; et al. Controlled growth and shape-directed self-assembly of gold nanoarrows. *Sci. Adv.* **2017**, *3*, e1701183.
201. Kalsin, A.M.; Fialkowski, M.; Paszewski, M.; et al. Electrostatic self-assembly of binary nanoparticle crystals with a diamond-like lattice. *Science* **2006**, *312*, 420–424.
202. Kahn, J.S.; Gang, O. Designer Nanomaterials through Programmable Assembly. *Angew. Chem., Int. Ed.* **2022**, *61*, e202105678.
203. Jana, A.; Jo, Y.; Im, H. Multicomponent perovskite superlattices. *Matter* **2021**, *4*, 2607–2609.
204. Mattiotti, F.; Kuno, M.; Borgonovi, F.; et al. Thermal Decoherence of Superradiance in Lead Halide Perovskite Nanocrystal Superlattices. *Nano Lett.* **2020**, *20*, 7382–7388.